Chemical Engineering Journal 513 (2025) 162755

Contents lists available at ScienceDirect

Chemical Engineering Journal

journal homepage: www.elsevier.com/locate/cej

A self-actuating and self-sensing microcantilever sensor modified by rGO-COOH@CuNPs@Ce-MOF nanocomposites for rapid detection of ALV-J

Yongbin Qin [a,b], Zichen Zheng [a,c], Wei Gu [d], Carla Bittencourt [c], Yani Jiang [a], Lifeng Zhang [b,*], Yixiang Bian [a,*]

[a] School of Mechanical Engineering, Yangzhou University, 196 Huayang West Road, Yangzhou 225127, China
[b] Graduate School of Engineering, Kyushu Institute of Technology, Kitakyushu 804-8550, Fukuoka, Japan
[c] Chimie des Interactions Plasma-Surface, Research Institute for Materials Science and Engineering, University of Mons, 20 Place du Parc, Mons 7000, Belgium
[d] School of Chemistry and Chemical Engineering, Yangzhou University, 180 Si-Wang-Ting Road, Yangzhou 225002, China

ARTICLE INFO

Keywords:
Nanocomposites
Redox properties
PZT
Self-actuating and self-sensing
Real-time tracking

ABSTRACT

Avian Leukosis Virus-J (ALV-J) poses significant challenges to poultry health and food safety, highlighting the need for innovative detection technologies due to existing limitations in detection time, sensitivity, and selectivity. This study presents a self-actuating and self-sensing microcantilever sensor that uses reduced graphene oxide functionalized with carboxylic groups, copper nanoparticles, and cerium-based metal–organic frameworks (rGO-COOH@CuNPs@Ce(III, IV)-MOF) nanocomposites to enhance signal amplification. The sensing platform design integrates a piezoelectric actuator and sensors, using both positive and inverse piezoelectric effects of piezoelectric ceramic (PZT) to facilitate real-time tracking via OpenCV. The fabrication process effectively combines the actuator and sensors, optimizing piezoelectric effects for improved sensitivity and rapid response. Signal amplification is achieved through the incorporation of rGO-COOH@CuNPs@Ce(III, IV)-MOF nanocomposites, which significantly enhance conductivity and dispersibility, promoting the formation of a conductive network with CuNPs. Additionally, Ce(III, IV)-MOF serves as a catalyst for the CuNPs, promoting electron transfer and enhancing the efficiency of antigen–antibody interactions. The sensor demonstrates a linear detection range from 2.1×10^{-1} to 1.0×10^{1} ng mL^{-1}, with a limit of detection (LOD) of 1.3×10^{-1} ng mL^{-1} and rapid detection capabilities, yielding results within seconds. Furthermore, it exhibits satisfactory selectivity, storage stability, and reproducibility, with a relative standard deviation (RSD) of 3.57 %. This self-actuating and self-sensing microcantilever sensor shows significant potential for the detection of ALV-J in clinical diagnostics.

1. Introduction

Avian Leucosis Virus (ALV) is a neoplastic infectious agent belonging to the retrovirus family, known for its high mutability. This virus can be categorized into 11 subgroups based on various characteristics, including envelope protein, host range, and cross-neutralization modes. Among these, the Avian Leukosis Viruses subgroup J (ALV-J) is particularly virulent, primarily causing malignant proliferation of hematopoietic cells and vascular tumors in chickens [1,2]. The emergence of ALV-J has resulted in increased poultry mortality, reduced production performance, and significant economic losses within the poultry farming industry, adversely affecting the quality and availability of poultry meat in the food supply chain. Therefore, the development of a detection sensor with high stability and selective specificity for ALV-J is crucial for ensuring food safety and supporting the sustainability of the poultry sector. Current detection methods for ALV-J include enzyme-linked immunosorbent assay (ELISA) [3], real-time quantitative polymerase chain reaction (qPCR) [4], cross-priming amplification (CPA) [5], and chromatography [6], among others. While these techniques are effective, they often require expensive equipment, complex operational protocols, and specialized personnel, which limits their practical application.

The microcantilever bioimmunosensor (MCBS) integrates piezoelectric ceramic-microcantilever (PZT-MC) technology with specific immunological reactions, offering significant research potential in food safety. The MCBS, developed from atomic force microscopy (AFM), biosensors, and surface stress effects, is characterized by high sensitivity and reproducibility [7]. When exposed to an external dynamic

* Corresponding authors.
E-mail addresses: zhang@elcs.kyutech.ac.jp (L. Zhang), yxbian@yzu.edu.cn (Y. Bian).

https://doi.org/10.1016/j.cej.2025.162755
Received 1 February 2025; Received in revised form 2 April 2025; Accepted 16 April 2025
Available online 19 April 2025

excitation voltage, the piezoelectrically driven resonant microcantilever sensor (MCS) responds dynamically in terms of charge and amplitude. Small molecule antigen–antibody interactions on the microcantilever surface induce conformational changes in the antibody, resulting in tensile stress and bending toward the binding surface. In contrast, interactions with larger molecules generate repulsive forces that cause the microcantilever to bend away from the binding surface [8–10]. Thus, the interactions between target molecules and probe molecules on the MCS surface lead to measurable changes in the charge and amplitude, facilitating detection. By using the positive and inverse piezoelectric effects of PZT, the target actuator, sensor, and microcantilever are integrated into a single device, resulting in the self-actuating and self-sensing microcantilever sensor (SASS-MS) [11,12]. Compared to the complex and costly optical lever readout systems used with MCS, the SASS-MS employs an OpenCV-based system for image processing and machine learning, along with a responsive charge output system, allowing for high-precision detection of target analytes through simplified operational protocols. Despite its potential, research on the SASS-MS is relatively limited compared to the MCBS, with no prior reports on its application for detecting ALV-J.

Several factors significantly influence the sensitivity of the SASS-MS, including the conductivity of the PZT-MC, the activity of antibodies, and the effectiveness of their immobilization. Nanomaterials such as copper nanoparticles (CuNPs), gold nanoparticles (AuNPs), and graphene oxide (GO) are commonly used as conductive dielectrics in sensing systems due to their large surface area, abundant active sites, and excellent conductivity [13–15]. Additionally, reduced graphene oxide with carboxyl groups (rGO-COOH) can be synthesized by modifying GO to increase carboxyl content, allowing for covalent conjugation with antibody molecules [16,17]. Incorporating nanomaterials as signal amplification composites onto the PZT-MC surface enhances the sensor's charge signal and amplitude. Moreover, metal–organic frameworks (MOFs), composed of metal ions and versatile organic ligands, exhibit large specific surface areas, porosity, and excellent catalytic properties, making them widely applicable for detection [18–20]. The oxidation states of cerium (Ce) can undergo rapid and reversible transitions between Ce^{3+} and Ce^{4+}, demonstrating exceptional redox properties, catalytic activity, and high electron transfer rates [21,22]. Ce-MOF facilitates interactions with nucleic acid sequences via hydrogen bonding, forming functional groups that enhance antibody recognition and immobilization [23]. The excellent catalytic activity of Ce-MOF, attributed to its semiconductor properties and redox capabilities, combined with its large specific surface area and porous structure, provides a large number of active sites for antibody loading [24–27]. To further enhance detection performance, antibody loading can be improved through the preparation of nanofiber film (NFF) using polyvinylidene difluoride (PVDF), which possesses piezoelectric properties. The NFF produced by electrospinning not only has a high specific surface area but also transforms the loading structure from "one-dimensional" to "three-dimensional" due to its high porosity and hierarchical architecture [28]. Additionally, nanomaterials such as rGO-COOH, Au nanoparticles, and NFF can undergo activation of carboxyl groups via EDC/NHS treatment, facilitating antibody coupling [8,28,29].

Our research group has systematically studied micro-scale piezoelectric devices, focusing on their fabrication, electromechanical coupling modeling, performance characterization, parameter testing, and integration with drivers and sensors [30–36]. In this study, we engineered a self-actuating and self-sensing microcantilever sensor based on rGO-COOH@CuNPs@Ce(III, IV)-MOF (rGCNCM) nanocomposites to detect ALV-J (Scheme 1). Initially, GO was modified to obtain rGO-COOH, which was subsequently mixed with synthesized nanomaterials, including CuNPs and Ce-MOF. This mixture was used to modify the PZT-MC, which had been sputter-coated with Au. Following this, EDC/NHS cross-linking agents were then used for the carboxylation treatment of Au and nanofibers to facilitate the covalent fixation of the monoclonal antibody 5D3 (Ab_{5D3}). Finally, we constructed an OpenCV real-time tracking system and a self-actuating and self-sensing system to evaluate the detection performance of the SASS-MS for ALV-J. The accuracy of the sensor was validated using enzyme-linked immunosorbent assay (ELISA). The sensor demonstrated high sensitivity, high integration, low cost, and real-time tracking capability for response signals, making it widely applicable in portable biological and chemical detection systems.

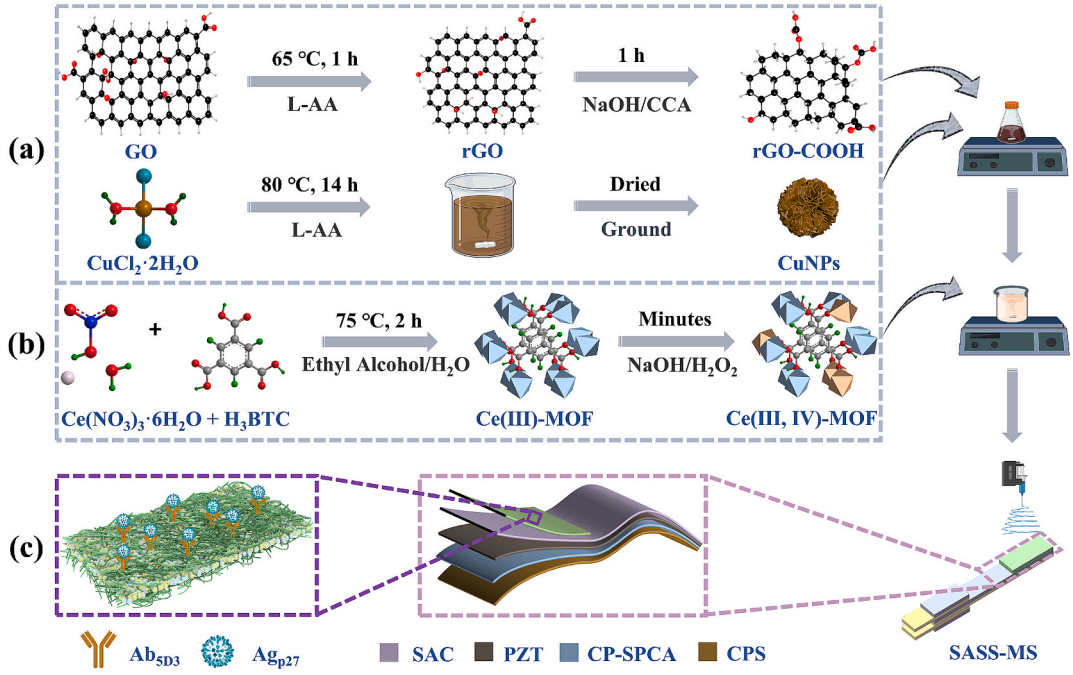

Scheme 1. The self-actuating and self-sensing microcantilever sensor for detecting ALV-J.

2. Experimental sections

2.1. Reagents and materials

The specific content can be found in the Supplementary Information.

2.2. Apparatus and characterization

The specific content can be found in the Supplementary Information.

2.3. The synthesis of rGO-COOH@CuNPs and Ce-MOF

The rGO-COOH@CuNPs nanocomposite was synthesized according to established methodologies [37–39]. Initially, 10 mg of graphene oxide (GO) was dispersed in 100 mL of deionized water, preparing a GO suspension (0.1 mg mL^{-1}). Subsequently, 100 mg of L-ascorbic acid (L-AA) was introduced into the suspension, and the pH was adjusted to 10 using ammonia solution ($NH_3{\cdot}H_2O$). The mixture was stirred for one hour at 65 °C, after which the resultant reduced graphene oxide (rGO) was collected via filtration through a 0.2 μm acetic acid fiber membrane. Following this, rGO was combined with a NaOH/chloroacetic acid (CAA) (m:m = 6:5) solution in a mass ratio of 1:11 and stirred at room temperature for one hour. The mixture was then filtered and dried in a vacuum oven to yield carboxyl-functionalized reduced graphene oxide (rGO-GOOH). In parallel, a solution of L-AA (25 mL, 1 M) was added to an aqueous solution of $CuCl_2{\cdot}2H_2O$ (25 mL, 0.2 M). The mixture was stirred at 80 °C for 14 h, followed by washing with deionized water and subsequent drying. Finally, rGO-GOOH (10 mL, 1 mg mL^{-1}) was combined with the CuNPs solution (10 mL, 1 mg mL^{-1}) at room temperature for 12 h to obtain the rGO-COOH@CuNPs nanocomposite.

The synthesis of the cerium-based metal–organic framework (Ce(III, IV)-MOF) was conducted following established protocols [22,40]. Initially, 2.1 g of H3BTC was added to a mixed solution of water and ethanol (20 mL, V: V = 1:1) and stirred thoroughly. Subsequently, 4.34 g of cerium nitrate hexahydrate ($Ce(NO_3)_3{\cdot}6H_2O$) was dissolved in 45 mL of deionized water and added to the H3BTC solution, which was stirred in a water bath maintained at 75 °C for 2 h. Upon cooling to room temperature, the resulting white precipitate was isolated via high-speed centrifugation, washed with deionized water and ethanol, and then dried in an oven at 70 °C for 12 h to obtain Ce(III)-MOF. Finally, 20 mg of Ce(III)-MOF (20 mg) was dispersed in 4 mL of deionized water, and a specific volume of $NaOH/H_2O_2$ (50 μL, NAHO-x) was added. After stirring for 2–5 min, the mixture was washed and dried, yielding a yellow Ce(III, IV)-MOF powder.

2.4. The fabrication of the SASS-MS

Initially, conductive silver paste was applied to the upper and lower surfaces of the PZT-MC and allowed to cure. The assembly was then placed in a thermostatic oil bath at 100 °C, where a polarization reaction was induced by applying a voltage of 1.5 kV using a pressure-resistant tester. After 60 min, the sample was allowed to cool to room temperature, removed, cleaned, and dried, resulting in a polarized PZT-MC preform. Subsequently, epoxy conductive adhesive (ECA) was uniformly deposited on one surface of the PZT-MC preform, and copper foil was affixed. The assembly was subjected to uniform pressure for 24 h to facilitate bonding. Finally, the assembly was completed using heat shrink tubing and ECA, with silver wire serving as a conductor for electrode output, resulting in the formation of the SASS-MS preform.

The target reaction zone (TRZ) of the SASS-MS preform was subjected to sputtering using an ion sputter for 10 s, resulting in a sputtered Au coating (SAC). A solution consisting of 2.5 g of PVDF was added to a DMF/Acetone mixture (10 g, m:m = 2:3), and stirred until fully dissolved. The rGCNCM nanocomposites (0.052 g, m:m = 1:1) were then incorporated into the solution, achieving a relative PVDF content of 2.0 wt%. This mixture was transferred into a syringe equipped with an 18 G needle (inner diameter of 0.86 mm), and electrospinning was conducted on the sensor's TRZ under environmental conditions (25 °C, 45 % relative humidity). The electrospinning apparatus operated at a feed rate of 0.8 mL h^{-1}, a spinning distance of 15 cm, a working voltage of 15 kV, and a drum rotation speed of 100 r min^{-1}. Following the cutting of the nanofiber film, the non-immunized state of the SASS-MS was obtained.

The TRZ on the non-immunized SASS-MS was immersed in an EDC/NHS solution (1 mM) for 2 h to activate the carboxyl groups of Au, rGO-COOH, and PVDF, at room temperature. After rinsing with PBS, the sensor's TRZ was immersed in an Ab_{5D3} solution (100 μL) and reacted at 4 °C for 3 h. The sensor was washed with PBS (0.2 M, pH = 7) to eliminate unbound Ab_{5D3}. Any unreacted carboxyl sites were subsequently blocked with BSA (100 μL, 1 %). Finally, following PBS washing, the immune-modified SASS-MS, incorporating rGCNCM nanocomposites, was stored at 4 °C.

2.5. The detection process of the SASS-MS

Initially, varying concentrations of the antigen p27 (Ag_{p27}, 50 μL) were placed on the TRZ of the SASS-MS and incubated at room temperature for 15 to 30 min. Subsequently, a sinusoidal alternating current with a frequency of 1 Hz and a voltage of 10 Vpp was used as the actuating signal. The sensing signal was collected as a charge signal via a data acquisition card and transmitted to LabVIEW. Additionally, real-time monitoring of the vibrations of the MC was conducted using OpenCV through the monitoring system. Ultimately, an analysis of the charge signal and amplitude of the SASS-MS at various Agp27 concentrations was performed, alongside an exploration of the SASS-MS potential for detecting real samples.

3. Results and discussion

3.1. Structural characterization of the nanocomposites

The morphology of the prepared nanomaterials was characterized using SEM and TEM (Fig. 1). GO exhibits a wrinkled appearance due to its significant layer stacking (Fig. 1a). This phenomenon can be explained by the Lerf-Klinowski model, which postulates that an irregular force distribution occurs when oxygen-containing functional groups on the surface basal plane (such as hydroxyl, epoxy groups) and at the edges (including carboxyl, carbonyl groups) interact with sp^3 carbon atoms, resulting in the formation of wrinkles [39,41]. Additionally, thermal treatment and drying may induce the aggregation or stacking of layers, which can adversely affect conductivity and dispersibility. Upon reduction with L-Ascorbic acid (L-AA), the surface of reduced graphene oxide (rGO) reveals increased roughness, with layers appearing fractured and aggregated, resulting in the formation of porous structures (Fig. 1b). This modification is primarily caused by the dissociation of oxygen-containing functional groups (hydroxyl, epoxy groups) within the basal plane or aromatic structure during the reduction reaction [42]. While the reduction reaction enhances the electrical conductivity of rGO, the loss of oxygen-containing functional groups, along with π-π conjugation and hydrophobic interactions, reduces its dispersibility [43,44]. Therefore, carboxylation treatment with Chloroacetic acid (CAA) is performed under weak alkaline conditions. After carboxylation, the layered and porous structure of rGO-COOH is significantly altered, resulting in a smoother surface with reduced wrinkling and markedly improved dispersibility (Fig. 1c). The carboxylation treatment introduces a substantial number of carboxyl functional groups to rGO-COOH, thereby enhancing its surface wettability, hydrophilicity, and electroactivity [45]. The morphology and distribution of the synthesized copper nanoparticles (CuNPs), including their aggregation, were characterized using SEM, as shown in Fig. 1d. The SEM images reveal that the CuNPs exhibit a uniform spherical structure with an average diameter of approximately 50.0 nm. The particles display smooth surfaces, relatively uniform distribution, and stable morphology, indicating the

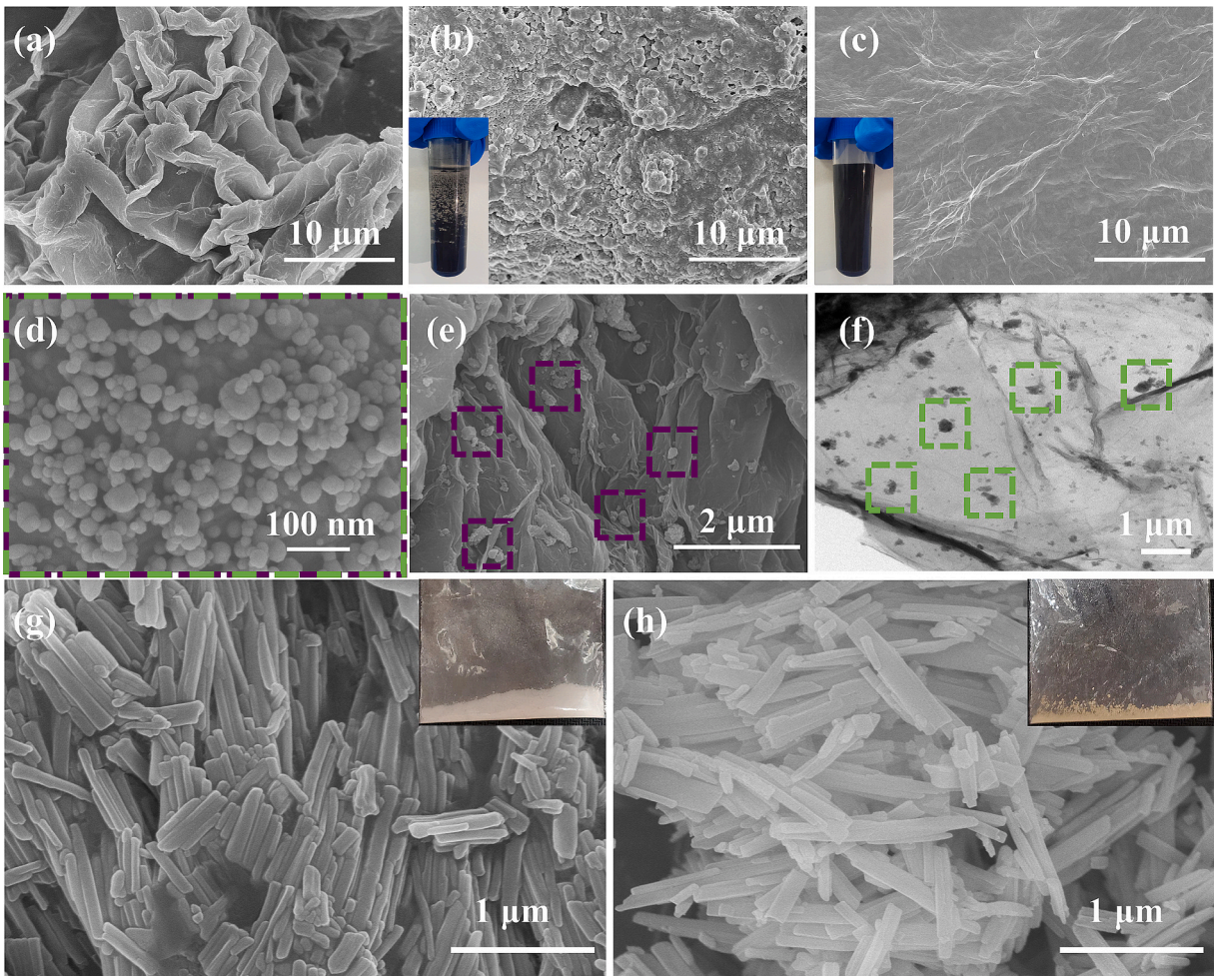

Fig. 1. A-e, g-h) sem images of go (a), rgo (b), rgo-cooh (c), cunps (d), rgo-cooh@cunps (e), ce(iii)-mof (g) and ce(iiii, iv)-mof (h). f) TEM images of rGO-COOH@CuNPs.

reliability of the synthesis process. The aggregated states of CuNPs enhance their structural stability and promote efficient attachment to rGO-COOH, contributing to the stability of the composite material. The significant attachment of CuNPs to the rGO-COOH surface, while maintaining the morphological integrity of the nanoparticles, was confirmed by SEM and TEM analysis following their integration with rGO-COOH (Fig. 1e and f). The adhesion of CuNPs to the rGO-COOH surface transforms its initially flat, two-dimensional structure into a three-dimensional configuration with microscale topography, enriching the surface morphology with a layered texture. SEM characterization reveals that Ce(III)-MOF exhibits a distinct nanorod morphology characterized by smooth edges. Upon reaction with NaOH/H_2O_2 (NAHO), a portion of Ce^{3+} is oxidized to Ce^{4+}, resulting in the transformation of the white Ce(III)-MOF into yellow Ce(III, IV)-MOF featuring a mixed oxidation state [22]. The microscopic structure of Ce(III, IV)-MOF retains the nanorod configuration, but its edges are sharper. The mixed valence states of Ce^{3+} and Ce^{4+} in Ce(III, IV)-MOF induce charge transfer transitions, allowing the material to absorb light over a broader visible range. Additionally, the interaction between valence states enhances electron delocalization, further influencing the optical properties of the material, resulting in its yellow appearance (Fig. 1g and h) [46].

The X-ray diffraction (XRD) patterns of GO before and after modification are presented in Fig. 2a. The diffraction peak of unprocessed GO at 11.19° corresponds to the (001) plane, while the diffraction peak at 42.3° corresponds to the (100) plane. Following the reduction of GO to rGO, a characteristic diffraction peak at 22.98° is observed, corresponding to the (002) plane. This indicates a structure with sp^2 hybridization similar to graphite, suggesting a reduction in the number of oxygen functional groups [39]. According to Bragg's Law ($2dsin\theta = n\lambda$, where d denotes the distance between crystal planes, θ represents the angle formed by the incident X-ray with the specific crystal plane, λ is the wavelength of the X-ray, and n denotes the diffraction order), the interlayer distance of rGO is reduced to 0.39 nm, compared to 0.79 nm for GO. Consequently, the interlayer interactions in rGO are strengthened, which may lead to an increased tendency for aggregation and difficulty in dispersion, corroborating the observations from SEM. The XRD diffraction of rGO-COOH reveals peaks at 27.37° (111), 31.70° (200), 45.45° (220), 56.47° (222), 66.22° (400), and 75.29° (420), which correspond to the residual NaCl following carboxylation treatment (consistent with PDF#99–000-1459). Furthermore, the diffraction pattern remains similar to that of rGO, indicating that the introduction of carboxyl groups does not significantly disrupt the rGO structure. The XRD pattern of rGO-COOH decorated with CuNPs (rGO-COOH@CuNPs) exhibits diffraction peaks at 43.17° (111), 50.13° (200), and 73.96° (220), attributed to CuNPs. This suggests the successful removal of NaCl and the effective attachment of CuNPs (consistent with PDF#98–000-0172).

FTIR spectra recorded before and after the modification of GO are illustrated in Fig. 2b. In the range of 3600 cm^{-1} to 3300 cm^{-1}, the intensity of the peaks associated with carboxyl groups decreases in the order of rGO-COOH, GO, and rGO, indicating a reduction in carboxyl group content following modification. Conversely, the carboxylation with Chloroacetic acid (CAA) significantly enhances the carboxyl group content, consistent with the results obtained from SEM and XRD.

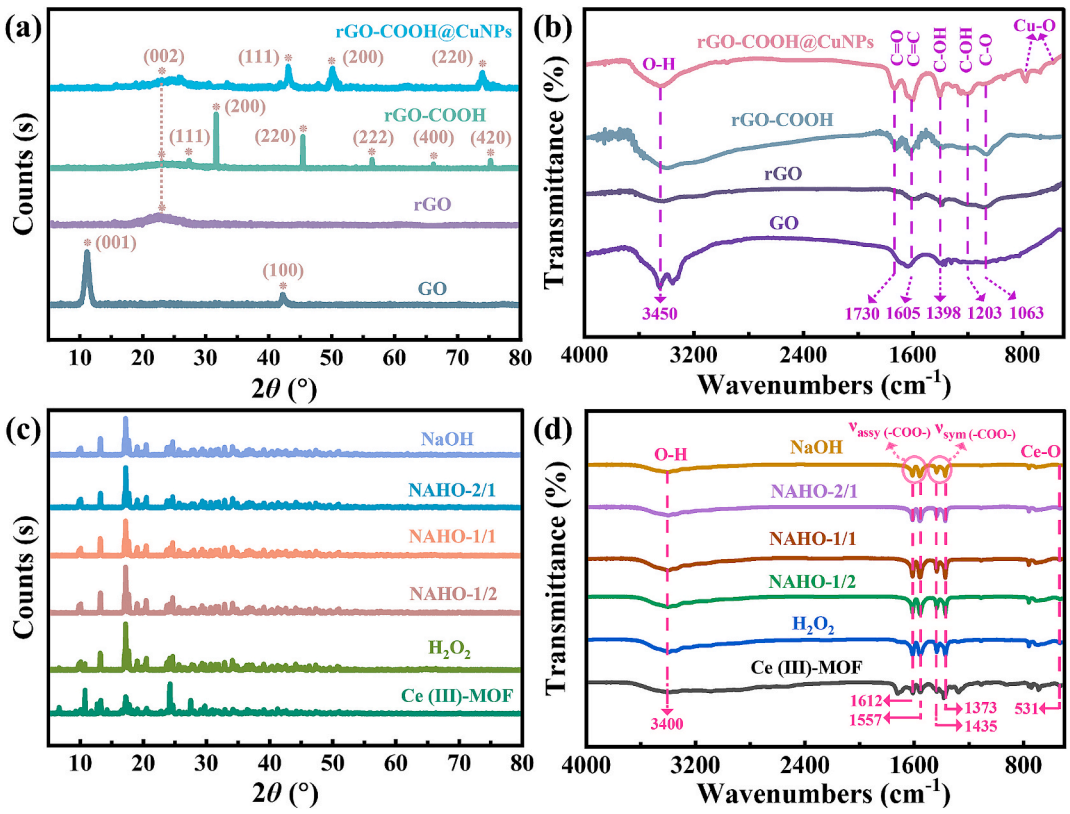

Fig. 2. a, c) XRD patterns and FTIR spectra of GO, rGO, rGO-COOH, and rGO-COOH@CuNPs. b, d) XRD patterns and FTIR spectra of Ce(III)-MOF and Ce(III, IV)-MOF under different oxidation conditions.

Additionally, the diffraction peaks in the ranges of 800 cm^{-1} to 750 cm^{-1} and 620 cm^{-1} to 500 cm^{-1} are attributed to Cu–O stretching vibrations, confirming the successful incorporation of CuNPs [47].

The XRD patterns and FTIR spectra of Ce-MOF are shown in Fig. 2c and Fig. 2d, respectively. The XRD patterns indicate that the Ce-MOF adopts a UiO-66-type structure characterized by narrow and intense diffraction peaks that reflect excellent crystallinity, consistent with the literature reported [24,48]. Moreover, the diffraction peaks of Ce(III)-MOF and Ce(III, IV)-MOF are similar, suggesting that the treatment with NAHO alters the valence states of some Ce ions without affecting the crystal structure of Ce-MOF. The FTIR spectra reveal characteristic peaks in the ranges of 1650 cm^{-1} to 1500 cm^{-1}, 1480 cm^{-1} to 1330 cm^{-1}, and 570 cm^{-1} to 500 cm^{-1}, corresponding to the asymmetric (ν_{assy} (–COO-)) and symmetric (ν_{sym} (–COO-)) stretching vibrations of the carboxylate ions, as well as the Ce-O stretching vibration [49]. Additionally, peaks in the range of 3500 cm^{-1} to 3300 cm^{-1} are associated with water molecules adsorbed on the surface of Ce-MOF.

3.2. *Performance analysis of the nanocomposites*

The XPS analysis of GO and rGO-COOH@CuNPs reveals the presence of the Cl 2p peak at 200.5 eV and the Cu 2p peak at 934.4 eV (Fig. 3a). The results are consistent with the XRD analysis, further confirming the decoration with CuNPs. The C1s core level spectra of GO and rGO-COOH were analyzed by XPS to assess the changes in functional groups due to modification. As illustrated in Fig. 3b, the principal peaks for both GO and rGO-COOH are centered at 284.8 eV, 286.9 eV, 287.3 eV, 288.6 eV, and 289.5 eV, corresponding to sp^2/sp^3 carbon (C=C or C–C), ether bonds (C-O-C), carbonyl groups (C=O), ester groups (O-C=O), and carboxyl groups (–COOH), respectively [50]. Notably, the carboxyl group content in modified rGO-COOH is significantly elevated at 22.9 %, compared to only 1.4 % in untreated GO. This indicates the successful introduction of carboxyl functional groups, which is consistent with prior characterization results. The Cu 2p XPS spectrum (Fig. 3c) displays peaks centered at 955.3 eV and 935.5 eV corresponding to the doublet Cu $2p_{1/2}$ and Cu $2p_{3/2}$, respectively. Additionally, a prominent peak at 944.3 eV is identified as the satellite peak of Cu^{2+}. The binding energies for the Cu $2p_{3/2}$ peak for Cu^{2+} and metallic Cu within the range of 932.2 eV to 932.9 eV cannot be distinguished [51]. Therefore, an analysis of Cu LM2 Auger peaks was performed. The Auger peak at 918.7 eV kinetic energy is associated with the presence of Cu (0) (Fig. S1) [52]. Therefore, the peak at 932.7 eV indicates the presence of metallic Cu. Collectively, the XRD and XPS results indicate that CuNPs are successfully attached to the surface of rGO-COOH, with minimal oxidation of copper occurring.

The investigation further demonstrates that the particle size of CuNPs decreases with increasing concentrations of L-AA. At concentrations of 0.5 M, 1.0 M, 1.5 M, and 2.0 M, the particle sizes of CuNPs are approximately 1274.8 nm, 759.4 nm, 281.6 nm, and 73.2 nm, respectively (Fig. 3d). The increase in L-AA concentration facilitates the reduction of more Cu^{2+} to zero-valent Cu, while the presence of surface oxides inhibits particle growth, resulting in smaller CuNPs [38]. Moreover, as the concentration of L-AA increases, the color of CuNPs transitions from gray (dark state) to a brighter hue, indicative of the match color. The phenomenon is attributed to the surface plasmon resonance effect of CuNPs, wherein changes in size influence the absorption and reflection of light, thereby resulting in different colors [53]. Through BET-specific surface area analysis, it is observed that an increase in L-AA concentration correlates with a decrease in the particle size of CuNPs, while the specific surface area and pore volume gradually increase. At a concentration of 0.5 M, the specific surface area and pore volume are measured at 3.1707 $m^2\ g^{-1}$ and 0.0150 $cm^3\ g^{-1}$, respectively. In contrast, at a concentration of 2.0 M, both the specific surface area and pore volume increase to 6.7848 $m^2\ g^{-1}$ and 0.0266 $cm^3\ g^{-1}$, as shown in Fig. 3e and Fig. 3f. The reduction in particle size contributes to an enhanced specific surface area and increased pore volume, promoting

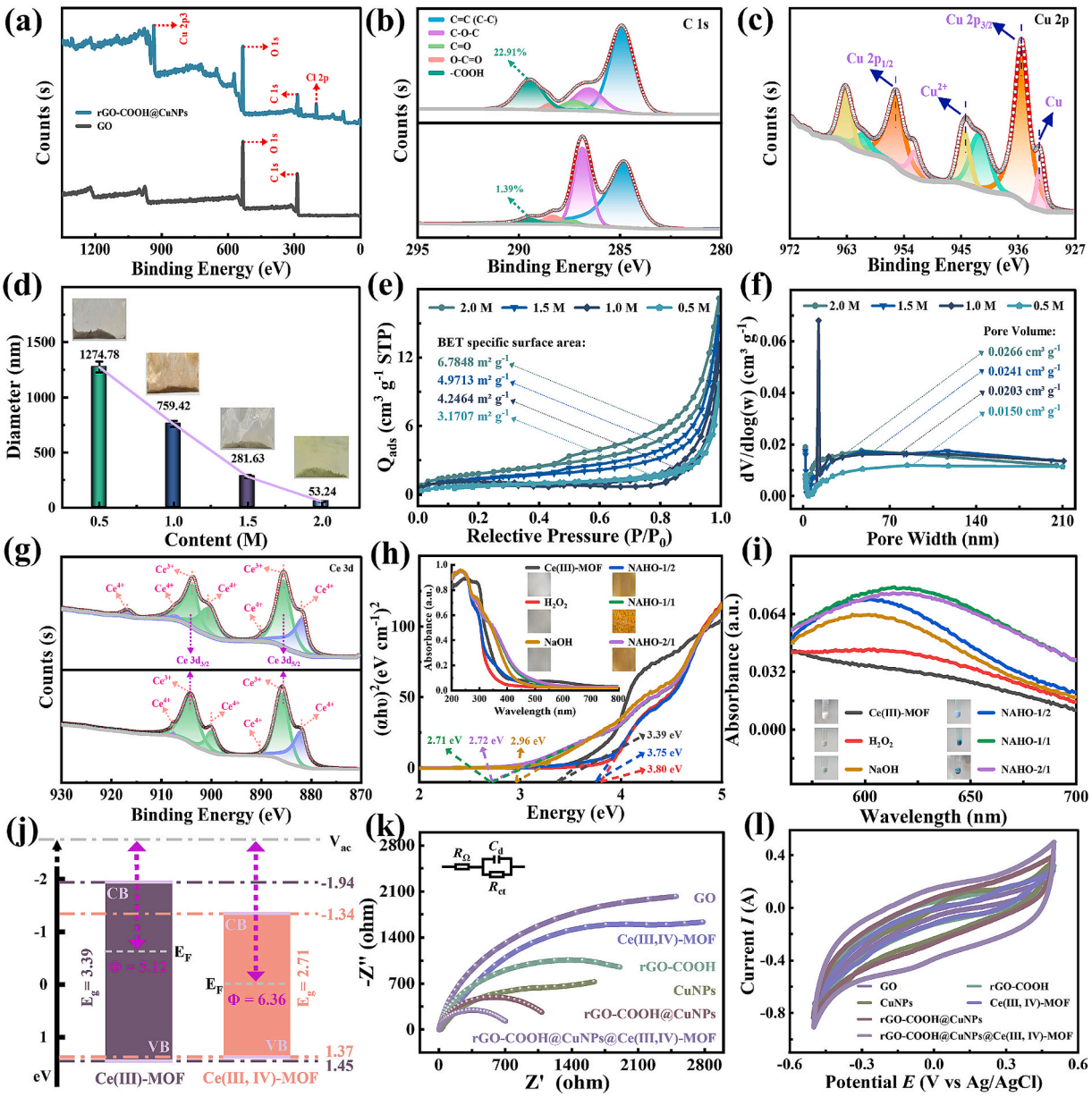

Fig. 3. A) the xps spectra of GO and rGO-COOH@CuNPs. b) The C 1 s core level XPS spectra of rGO-COOH@CuNPs. c) The Cu 2p XPS spectra of rGO-COOH@CuNPs. d-f) The particle size (d), specific surface area (e), and pore volume (f) of CuNPs treated with different concentrations of L-AA. g) The Ce 3d core level XPS spectra of Ce(III, IV)-MOF under different oxidation conditions. h-i) The UV–vis diffuse absorbance spectra, the band gap energies (h), and the catalytic activity (i) of Ce(III)-MOF and Ce(III, IV)-MOF under different oxidation conditions. j) The energy band structure of Ce-MOF. k) Impedance analysis of the nanocomposites. l) Electrical conductivity analysis of the nanocomposites.

the uniform development of fine crystals and enhancing both electrical conductivity and surface energy [51,54].

The analysis of the Ce 3d core level XPS spectra for the Ce-MOF reveals a distinct structure characterized by two multiplet features (ν and u) corresponding to the spin–orbit split $3d_{5/2}$ and $3d_{3/2}$ core levels (Fig. 3g) [22]. The peaks centered at 885.5 eV and 903.9 eV are attributed to Ce^{3+}, while the peaks centered at 882.0 eV, 890.2 eV, 900.5 eV, 907.5 eV, and 916.8 eV are indicative of Ce^{4+}. The results suggest that this Ce-MOF is composed of mixed valence states.

When the concentration ratio of NAHO is varied, the macroscopic morphology of the resulting Ce-MOF changes. Specifically, for NAHO ratios of pure NaOH, 1:2, 1:1, 2:1, and pure H_2O_2, a color transition is observed, progressing from milky white to yellow and subsequently to light hue, as shown in Fig. 3h. Notably, at a 1:1, the Ce-MOF displays a distinctive appearance characterized by a pure yellow flocculent structure. Analysis of the UV–visible diffuse absorbance spectra (Fig. 3h) reveals that the absorption edges of Ce-MOF, following various NAHO oxidative modifications, are approximately located at 332.9 nm (Ce(III)-MOF), 428.8 nm (pure NaOH), 435.3 nm (1:2), 467.7 nm (1:1), 459.4 nm (2:1), and 335.3 nm (pure H_2O_2). These observations indicate that when the reaction involves only NaOH or H_2O_2, the absorption edge of Ce-MOF remains relatively low. Conversely, the participation of both NaOH and H_2O_2 in defined proportions results in a redshift of the absorption edge, suggesting an enhancement in electron transfer capability [55,56]. Further analysis of UV–vis spectra allows for the determination of the band gap value of the samples using the Kubelka-Munk formula (Equation (1)).

$$\alpha h\nu = A(h\nu - E_g)^{n/2} \quad (1)$$

α, h, ν, A, and E_g represent the absorption coefficient, Planck constant,

incident light frequency, proportionality coefficient, and band gap energy, respectively [57].

The band gap of Ce(III)-MOF is 3.4 eV, whereas the band gap of Ce (III, IV)-MOF after modification via NAHO-1/1 is reduced to 2.7 eV (Fig. 3h). This reduction may be attributed to the formation of impurity energy levels, which enhance the electron transition ability. Additionally, the band structures of Ce-MOF can be elucidated through VB-XPS and Tauc plots (Fig. 3j), with a detailed analysis provided in Fig. S2 and Note 1. The work function of the modified Ce(III, IV)-MOF is recorded at 6.36 eV, an increase from the 5.12 eV associated with Ce (III)-MOF. This increase contributes to enhanced built-in electric fields and higher electron concentrations, thereby improving its electron transport capability.

The catalytic activity of the samples was assessed by mixing them with the chromogenic substrate TMB (Fig. 3i) [58,59]. At a 1:1 NAHO ratio, the reaction proceeds rapidly, yielding pure blue. During this process, Ce^{3+} is swiftly oxidized to Ce^{4+}, resulting in the formation of blue oxTMB. The UV–vis spectra indicate that the sample modified with NAHO-1/1 shows the optimal catalytic activity. This observation highlights the influence of the NaOH to H_2O_2 ratio on the oxidation states ratio (Ce^{3+}/Ce^{4+}) of Ce(III, IV)-MOF, which in turn affects electron transfer efficiency and catalytic activity in Ce-MOF.

The electronic transfer performance of the rGCNCM nanocomposites was evaluated using electrochemical impedance spectroscopy (EIS) and cyclic voltammetry (CV) techniques (Fig. 3k, l). Nyquist plots show that the rGCNCM nanocomposites exhibit the smallest semicircle diameter, indicating the lowest charge transfer resistance (Rct) and enhanced charge transfer rate. The significant decrease in Rct suggests that the introduction of CuNPs, together with rGO-COOH, contributes to the formation of a highly conductive network, thereby enhancing the charge transfer rate and electron mobility. In contrast, Ce(III, IV)-MOF displays relatively higher impedance, suggesting that its intrinsic conductivity is limited. However, the incorporation of Ce(III, IV)-MOF further reduces Rct, implying the presence of additional electron pathways and contact points within its structure that facilitate charge transfer. The CV results further confirm these findings. The rGCNCM nanocomposites electrode exhibits higher current response, reflecting its strong electron transport capability and high redox activity. CuNPs display typical reversible redox behavior, which promotes rapid electron exchange, while the Ce^{3+}/Ce^{4+} redox couple in Ce(III, IV)-MOF in Faradaic reactions further enhances redox performance. Additionally, the porous framework of Ce (III, IV)-MOF facilitates fast electrolyte ion diffusion, accelerates charge transport, and provides numerous active sites for redox reactions. Therefore, the rGCNCM nanocomposites are highly suitable for application in conductometric sensors to improve detection sensitivity.

3.3. Preparation of the SASS-MS and construction of the detection system

3.3.1. Design and fabrication of the SASS-MS

The detection methodologies employed for microcantilever sensors can be categorized into static and dynamic techniques. The static approach primarily uses optical methods to measure the displacement or deflection of the cantilever beam. In contrast, the dynamic method involves instrumental analysis to detect parameters such as amplitude, resonance frequency, and charge signals. However, the static method is characterized by lower accuracy and a significant stabilization period for sensor output and is unsuitable for applications requiring real-time responses.

Initially, wires were connected to the upper and lower surfaces of the PZT for piezoelectric testing, revealing no vibration or bending deformation (Fig. 4a1). This lack of response is attributed to the disordered crystal structure of PZT, where the internal electric dipole moments are randomly oriented, preventing charge separation and consequently resulting in the absence of a piezoelectric effect. To improve the crystalline structure of PZT, a highly controllable method involving a high-temperature oil bath was used for polarization (Fig. 4a2). To ensure the effective application of voltage, uniform transmission of voltage within the PZT, and uniform distribution on the surface during the polarization process, conductive silver paste was coated on the upper and lower surfaces of the PZT. The application of conductive silver paste improved the contact performance between the electrode and PZT, reduced the resistance between the electrode and PZT, minimized energy loss during polarization, and achieved a more uniform polarization effect. These enhancements resulted in improved piezoelectric effect, stability, and energy transmission efficiency of the PZT. The assembly of the polarized PZT yielded the SASS-MS preform with dimensions of 4.0 × 0.6 × 0.2 mm, as shown in Fig. 4a3 and Fig. 4b. The overall cantilever beam structure comprises piezoelectric ceramics and copper foils (Fig. 4b and Fig. 4c). At the fixed end, two copper foils served as electrodes integrated into the piezoelectric ceramic, while the corresponding surface

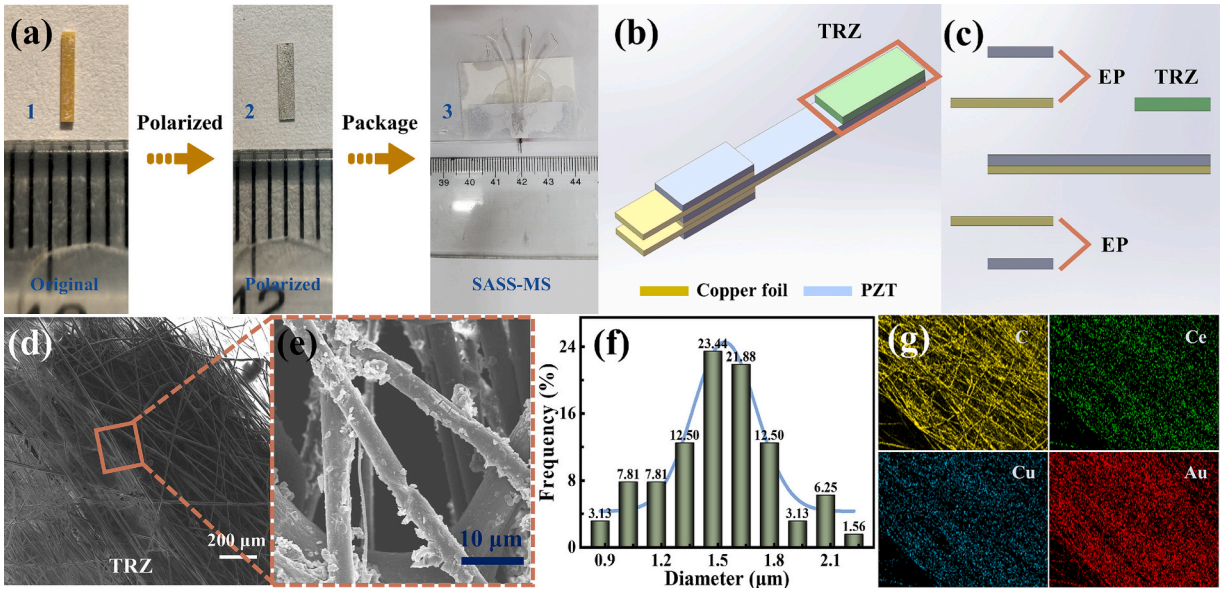

Fig. 4. A) polarization of the pzt and preparation of the sass-ms. b) the three-dimensional model diagram of the SASS-MS. c) The mechanism diagram of the SASS-MS. d) SEM images of the SASS-MS reaction area. e) Attachment status of the rGCNCM composites in nanofibers. f) Diameter distribution diagram of nanofibers. g) The EDS mapping analysis of the nanofiber film.

positions of the piezoelectric ceramic also function as electrodes, thereby creating two electrode pairs (EP), namely the upper surface EP and the lower surface EP on the fixed end (Fig. 4c). Upon applying an alternating voltage to one of the electrode pairs, the cantilever beam undergoes vibration deformation due to the inverse piezoelectric effect, while the other electrode pair generates corresponding charges as a result of the piezoelectric effect. This configuration enables dynamic and real-time detection of the sensor performance based on the amplitude of the cantilever beam vibration and the generated charge. Compared with traditional piezoelectric microcantilevers, optical (optical lever method), capacitive, and piezoresistive sensors, the SASS-MS developed in this study adopts a vertically layered sandwich structure. The bottom piezoelectric layer is used for actuation, the middle microcantilever beam for mechanical vibration response, and the top piezoelectric layer for electrical signal sensing. Traditional microcantilever sensors often rely on single-parameter detection methods such as the optical lever technique, which limits performance. In single-layer piezoelectric structures, actuation and sensing share the same material, leading to signal interference and reduced precision and reliability. Additionally, direct excitation signal input may cause overload, damage, and coupling effects, compromising stability. The SASS-MS eliminates signal interference, significantly improving stability while enabling multi-parameter detection based on vibration amplitude, frequency, and electrical signals, thereby enhancing detection accuracy and reliability. Compared with optical sensors, it does not require complex optical systems, facilitating miniaturization and array integration; compared with capacitive sensors, it is unaffected by humidity and electrolytes, with a simpler fabrication process; compared with piezoresistive sensors, it offers a higher signal-to-noise ratio. In summary, the SASS-MS demonstrates significant advantages in interference resistance, signal stability, portability, integration, and multi-parameter detection.

To enhance the performance of the sensor, nanocomposites were used for surface modification as a strategy for signal amplification. This approach aims to increase the number of reactive sites between the sensor and target analyte, thereby improving reaction efficiency and detection sensitivity. The sensing element, TRZ, was treated via spray coating and electrospinning (Fig. 4d). Spray coating not only enhances the microscale surface roughness of the PZT but also improves charge transfer efficiency between the reaction layer and the sensor. Concurrently, electrospinning facilitates the formation of a three-dimensional porous reaction structure, which increases the loading capacity of the nanocomposites and promotes enhanced adsorption and catalysis activity of reactants, thereby augmenting signal amplification performance [60]. Upon magnification, irregular protrusions and adherences on the surface of nanofibers were clearly observable, indicating the stable capacity of the nanofibers to support the rGCNCM nanocomposites (Fig. 4e). The smaller diameter of nanofibers facilitates the attachment and exposure of rGCNCM on their surfaces, thereby increasing the number of reactive sites and enhancing the interaction with the reactants, which in turn improves reaction efficiency. With an average diameter of approximately 1.51 μm, the nanofibers exhibit a larger specific surface area, increasing contact points and attachment areas with rGCNCM (Fig. 4f). Furthermore, the porous structure enhances the loading capacity for reactants, such as antigens and antibodies. Energy dispersive spectroscopy EDS mapping analysis reveals the presence and uniform distribution of elements such as C, Ce, Cu, and Au, further confirming the successful attachment of rGCNCM on the nanofibers (Fig. 4g).

3.3.2. Construction of the detection platform

A detection platform, designated as SASS-MS, was developed based on the characteristics of the fabricated sensor, which is both self-

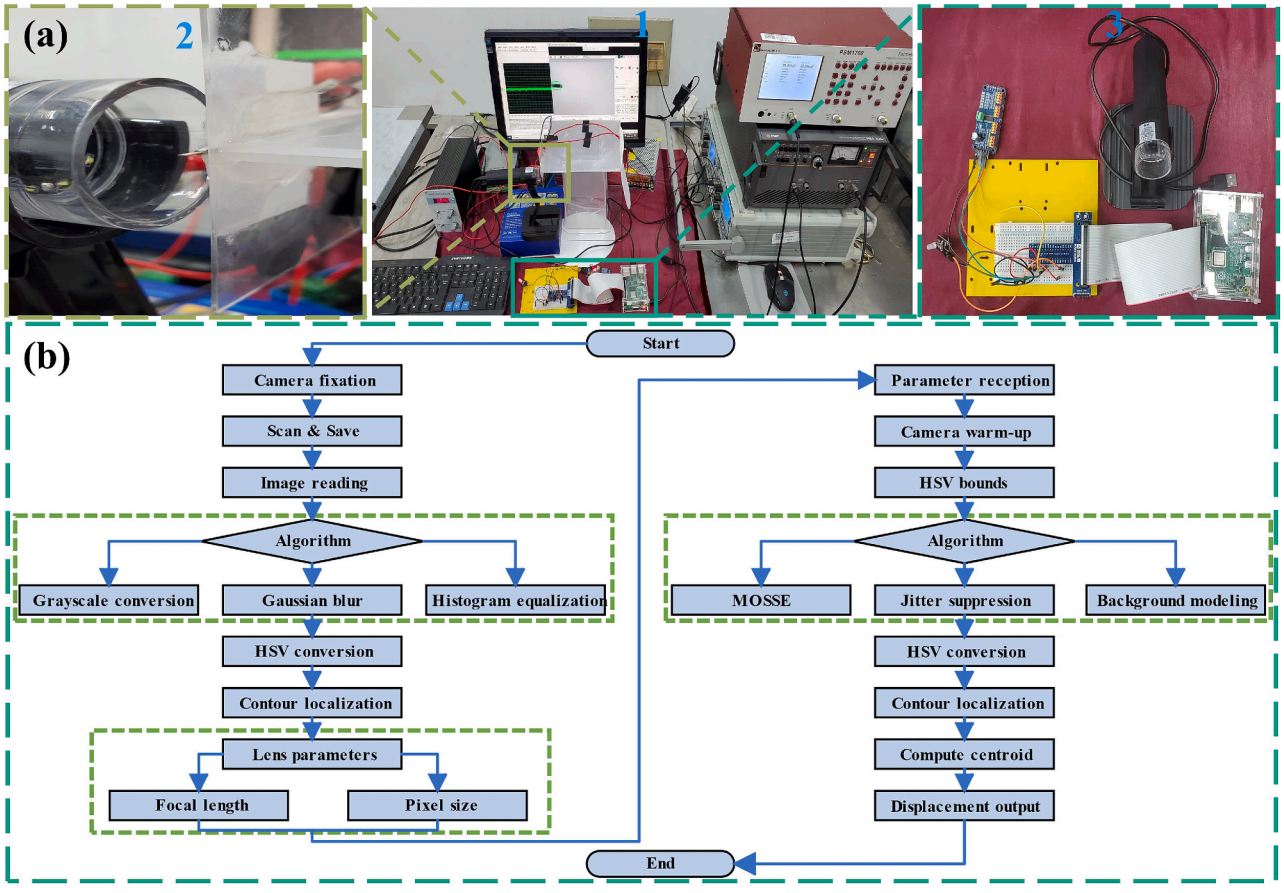

Fig. 5. A) construction diagram of multifunctional detection platform. b) flowchart of algorithm operation for real-time tracking system.

actuating and self-sensing, as shown in Fig. 5a1 and Fig. S3. The platform comprises two primary components: the actuating system and the sensing system, thereby achieving self-actuating and self-sensing of the sensor. The actuating system consists of the Frequency Response Analyzer (FRA) that generates the input frequency, a Power Amplifier (PA) that provides the input voltage, and a Piezoelectric Ceramic Controller (PCC) that delivers the alternating electrical signal, serving as the excitation signal. The sensing system is divided into two segments: charge reading and displacement reading. The "charge reading" components include a Quasi-Static Charge Amplifier (QSCA) for converting voltage to charge output, a Data Acquisition Card (DAC) for signal acquisition, and LabVIEW software for receiving and graphically representing the signals. The "displacement reading" segment comprises a high-magnification camera (up to 1000x) and the OpenCV Vision Development Kit, which captures real-time displacement of the microcantilever (MC) (Fig. 5a2 and 5a3). The traditional detection methods used in microcantilever sensors, such as the optical lever method and capacitive detection method, present various limitations. The optical lever method is highly sensitive to environmental conditions and requires complex tuning, while the capacitive detection method is susceptible to electromagnetic interference, leading to complex signal processing. In contrast, the SASS-MS detection platform is characterized by low construction cost, resistance to environmental interference, and real-time monitoring capabilities, thus saving time 0069n assessing experimental feasibility. Furthermore, this platform is adaptable for use with various piezoelectric sensors, including piezoelectric fiber sensors, enhancing its versatility.

The programming and functional implementation of the real-time tracking system are shown in Fig. 5b. This system is divided into three phases. In the initial phase, a camera scans the SASS-MS to capture the corresponding image. The second phase involves executing image processing algorithms to determine camera focal lengths and pixel dimensions. Accuracy and success rate in image processing are improved through the application of algorithms such as grayscale conversion (to highlight features), Gaussian blur (for noise reduction), and histogram equalization (to enhance image features). In the third phase, a program is executed to track the motion trajectory of the SASS-MS using the camera. This process enables rapid, accurate, and stable tracking of the MC-SASS motion through the implementation of algorithms such as MOSSE (for high precision, fast-tracking), jitter suppression (to eliminate vibration effects caused by the environment), and background modeling (to reduce external interference). Analysis conducted with TRACKER software indicates a strong correlation between sensor displacement data and data obtained from the real-time tracking system, thereby validating its applicability for experimental investigations. The operating procedure of this detection platform is as follows: First, the input frequency and peak-to-peak voltage of the alternating voltage are configured via the FRA and PA in the actuating system, followed by the input of the alternating voltage signal through the PCC. Subsequently, the QSCA converts the voltage signals feedback from the sensor into charge signals, which are then processed by DAC. Using the LabVIEW software, these signals were transformed into a two-dimensional image, enabling the visualization of the charge signals. Concurrently, OpenCV facilitates real-time tracking of the MC vibration through the camera as per the programmed instructions, with the displacement data being recorded by the Spyder software on the computer. Finally, a dynamic response model is established based on the detected substance, the feedback charge signals, and displacement signals. The real-time tracking system enables dynamic response analysis, real-time feedback control, and fault detection, thereby improving sensor performance, accuracy, and reliability.

3.3.3. Performance testing

To evaluate the detection performance of the SASS-MS, the sensor was tested on the designated platform. Under conditions of low frequency and a fixed input voltage of 10.0 Vpp, the SASS-MS was assessed in different states to determine the potential of the rGCNCM attachment as a signal amplifier. The results shown in Fig. 6a indicate that as the number of chemical elements in the nanocomposites increases, both charge and displacement signals recorded by the detection platform exhibit a corresponding increase. Notably, when the rGCNCM is attached to the sensor surface, the detection signal reaches its peak, approximately 3.72 times greater than the original, thereby confirming the efficacy of rGCNCM as a signal amplifier.

Furthermore, the detection performance of the platform was examined under both low-frequency and high-frequency conditions. In the low-frequency regime, the output charge remained stable in relation to the input voltage, with the output frequency demonstrating a consistent linear relationship with variations in input frequency (Fig. 6b and Fig. S4). At an input frequency of 1.0 Hz, the sensor displacement data obtained from the real-time tracking system achieved its maximum value before gradually diminishing. Investigations revealed that the tracking accuracy of the camera, which is not a high-speed model, becomes compromised at elevated vibration frequencies of the microcantilever (MC). In high-frequency conditions, while maintaining a constant input voltage, the output charge exhibited variations corresponding to changes in frequency (Fig. 6c and Fig. S5). The PZT demonstrates both a positive piezoelectric effect (the conversion of electrical signals into mechanical motion) and an inverse piezoelectric effect (the conversion of mechanical motion into electrical signals) [61]. In the context of the inverse piezoelectric effect, the correlation between the feedback charge intensity and vibration frequency is influenced by the ratio of the vibration frequency to the natural frequency of the PZT. During low-frequency operation, the vibration frequency of the PZT remains significantly below its natural frequency. This allows ample time for the material to respond to alterations in the electric field induced by frequency changes. Consequently, the feedback charge intensity is linearly related to the vibration amplitude (i.e., the excitation voltage intensity of the sensor) and remains independent of vibration frequency. Conversely, under high-frequency conditions, the vibration frequency approaches or exceeds the inherent frequency of the PZT. In this scenario, the molecular structure is unable to deform rapidly in response to changes in the electric field, resulting in incomplete charge, accumulation, and release. Thus, the charge generated by the inverse piezoelectric effect becomes frequency-dependent, losing its correlation with the excitation voltage intensity. As a result, the input frequency was set to 1.0 Hz in the following experiments.

3.4. Detection performance of the SASS-MS

Under optimized conditions, with a voltage of 10.0 Vpp and a frequency of 1.0 Hz, the developed detection platform was utilized to assess the performance of the SASS-MS in the identification of ALV-J. An increase in the concentration of ALV-J resulted in a corresponding rise in both the sensed charge intensity and the vibration displacement of the microcantilever (MC). Notably, the concentration of ALV-J exhibited a linear correlation with these two parameters (Fig. 7a). The linear regression equation for the sensed charge with the concentration of ALV-J is expressed as: $y = 0.0749x + 1.0624$, with an R^2 value of 0.9986. Similarly, the equation for the vibration displacement relative to the concentration of ALV-J is: $y = 0.1059x + 0.2399$, yielding an R^2 value of 0.9975. These findings indicate a robust linear correlation between both the sensed charge and displacement with the concentration of ALV-J. The regression coefficient ($k = 0.1059$) for the standard calibration curve of the displacement is significantly greater than that for the sensed charge ($k = 0.0749$), suggesting that displacement is a more sensitive parameter for detecting ALV-J concentration. A three-dimensional graph was also generated to illustrate the relationship among the concentration of ALV-J, the sensed charge, and the displacement; however, it should be noted that this representation does not constitute a three-variable calibration curve (Fig. 7b). The use of this graph for ALV-J detection may introduce substantial errors through the "Interpolation-

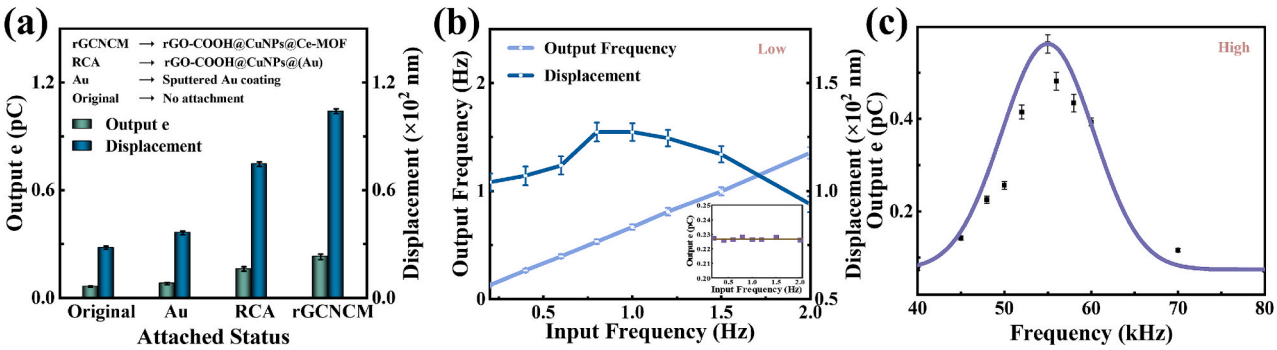

Fig. 6. A) signal amplification performance of rGCNCM nanocomposites. b) Detection system under low-frequency state (0.2 ~ 2.0 Hz). c) Detection system under high-frequency state (40.0 ~ 80.0 kHz).

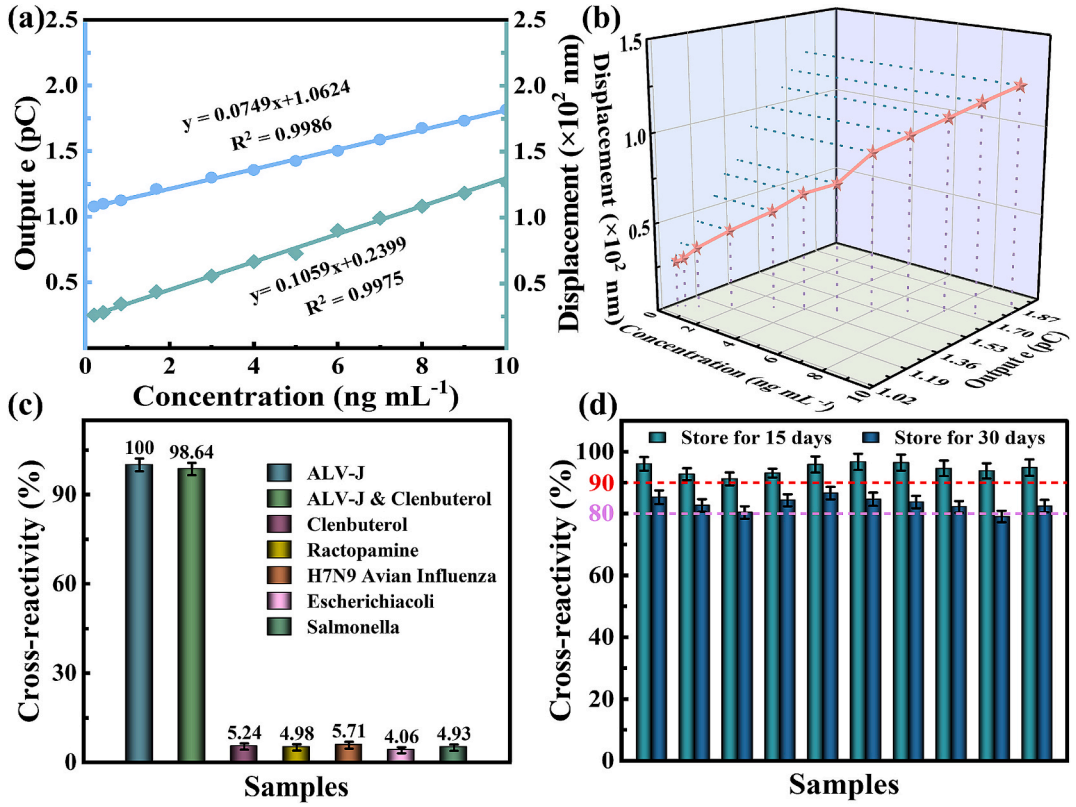

Fig. 7. A) the standard calibration curve for determination of alv-j. b) three-dimensional relationship diagram of concentration, charge, and displacement. c) detection specificity. d) storage stability.

Draw Lines-Extraction" method. Consequently, employing displacement as the detection parameter for ALV-J is recommended. Furthermore, the limit of detection (LOD) was determined using the signal-to-noise ratio method (S/N = 3), as presented in Equation (2). In this context, the linear detection range of the sensor spans from 2.1×10^{-1} to 1.0×10^{1} ng mL^{-1}, with a LOD is 1.3×10^{-1} ng mL^{-1}. Furthermore, the relatively smaller area of the TRZ of this sensor results in a lower antigen–antibody load, which, facilitated by nanocomposite catalysis, enhances the binding rate of antigen–antibody, the established detection platform allows for results to be obtained within seconds, in contrast to the 2 to 3 h typically required for ELISA testing. This underscores the rapid detection capability of the sensor. When compared to previous studies (Table 1), this sensor demonstrates reduced detection time, lower LOD, and an adequate linear range, thereby indicating superior detection sensitivity.

Table 1
Comparison of the performance of this sensor with others reported in the literature.

NO.	Incubation / Testing time	Linear range	LOD	References
1	45 mins / few mins	$10^{2.0}$ to $10^{4.0}$ $TCID_{50}$ mL^{-1}	$10^{1.93}$ $TCID_{50}$ mL^{-1}	[62]
2	20 mins / 10 mins	Around 2 mg/mL	–	[63]
3	60 mins / 15 mins	1.3×10^{2} to 5.0×10^{1} ng mL^{-1}	6.3×10^{0} ng mL^{-1}	[64]
4	30 mins / few mins	1.0×10^{0} to 2.0×10^{3} ng mL^{-1}	0.1×10^{0} ng mL^{-1}	[65]
5	15–30 mins / few seconds	2.1×10^{-1} to 1.0×10^{1} ng mL^{-1}	1.3×10^{-1} ng mL^{-1}	This work

$$LOD = \frac{3\sigma_{blank}}{k} \quad (2)$$

where σ is the standard deviation of the blank samples (n = 3), and k is the slope of the linear calibration curve between the response signal and the analyte concentration.

After infection with ALV-J, poultry chickens exhibit various clinical signs, including abnormal behavior, lethargy, and potentially infectious diarrhea. These symptoms may also be associated with other substances such as Clenbuterol, Ractopamine, H7N9 Avian Influenza, Escherichia Coli, and Salmonella. To investigate the selective specificity of the SASS-MS for ALV-J, potential interferents, including Clenbuterol, Ractopamine, H7N9 Avian Influenza, Escherichia Coli, and Salmonella, were selected as interferents. The displacement signal generated by the SASS-MS during ALV-J detection was established as the standard value (100 %), and variations in the displacement signal following the detection of different antigens were analyzed. The displacement signals corresponding to these interferents were notably less pronounced compared to that of ALV-J, demonstrating the excellent specificity of the SASS-MS, as illustrated in Fig. 7c.

To assess the long-term storage stability of the SASS-MS, tests were conducted after stored periods of 15 days and 30 days. It was observed that the detection performance gradually declined with extended storage; however, over 90 % of the initial performance was retained after 15 days, and more than 80 % was maintained after 30 days, as shown in Fig. 7d. The positive and inverse piezoelectric effects of the SASS-MS preform can remain stable for several months or even years, thus preserving its actuation and sensing capabilities over time [66]. Therefore, the prevention of antibody and antigen denaturation or deactivation is crucial for ensuring long-term storage stability. These results indicate that the SASS-MS has satisfactory storage stability.

The reproducibility of the SASS-MS was further evaluated by preparing ten identical sensors to detect the same concentration of ALV-J (1.00 ng mL^{-1}). The detection recovery of the SASS-MS ranges from 94.58 % to 104.13 %, with a relative standard deviation (RSD) of 3.57 % (n = 10), as shown in Table S1 and Equation (S3). These results confirm that the SASS-MS has good reproducibility.

3.5. The SASS-MS working mechanism and signal amplification mechanism

The operational principles of the SASS-MS, along with the signal amplification, are shown in Fig. 8. Untreated PZT does not exhibit charge separation or polarization phenomena, resulting in the absence of piezoelectric properties. During the polarization process, the application of high temperature and high electric field increases the kinetic energy of atoms and molecules within the PZT, leading to a modification in its crystal structure [67]. Additionally, the application of high voltage generates an external electric field around the PZT, causing internal charges to be influenced and redistributed. This redistribution results in the rearrangement of internal polar molecules or electric dipoles, accompanied by the generation of charges. In the conversion of mechanical to electrical energy, lattice distortion induces non-central symmetry in the lattice framework, prompting the displacement of electric dipoles. This displacement results in the separation of positive and negative charges, thereby manifesting piezoelectric properties.

In dynamic measurement methodologies, the integration of an actuator capable of generating excitation with a microcantilever into a single device is referred to as a self-actuating microcantilever sensor. When this sensor is integrated with the microcantilever as a single device, it is referred to as a self-sensing microcantilever sensor. If the actuator, sensor, and microcantilever are integrated into a single device, it is referred to as the SASS-MS. Upon application of voltage to the electrode pair of the PZT on the lower surface (P_L), the PZT on the upper surface (P_U) undergoes telescopic deformation due to the reverse piezoelectric effect, resulting in bending deformation of the entire microcantilever. When alternating voltage is applied, the microcantilever experiences bending vibration. Concurrently, the PZT on the upper surface generates corresponding electric charges on its electrode pair due to the inverse piezoelectric effect. This establishes a sensing model based on the charge generated by the PZT on the upper surface, the vibration amplitude of the microcantilever, and the concentration of the analyte, thereby facilitating the development of the SASS-MS. In comparison to the optical lever and capacitance methods in microcantilever sensors, the self-actuating and self-sensing detection platform of the SASS-MS offers significant advantages, including low cost, high efficiency, sensitivity, precision, and real-time monitoring capabilities. Consequently, the SASS-MS exhibits significant advantages in dynamic measurement methods.

The attachment of CuNPs to the surface of rGO-COOH involves processes such as physical adsorption and chemical binding. This includes surface adsorption driven by van der Waals forces, electrostatic interactions between oppositely charged species, and the functionalization of carboxyl groups. The layer-by-layer stacking of rGO-COOH creates a three-dimensional structure with continuous conductive channels, while CuNPs interconnect to form a conductive network. This network enhances the continuity of the conductive layer on the PZT surface, thereby facilitating electron transfer between layers and improving overall conductivity.

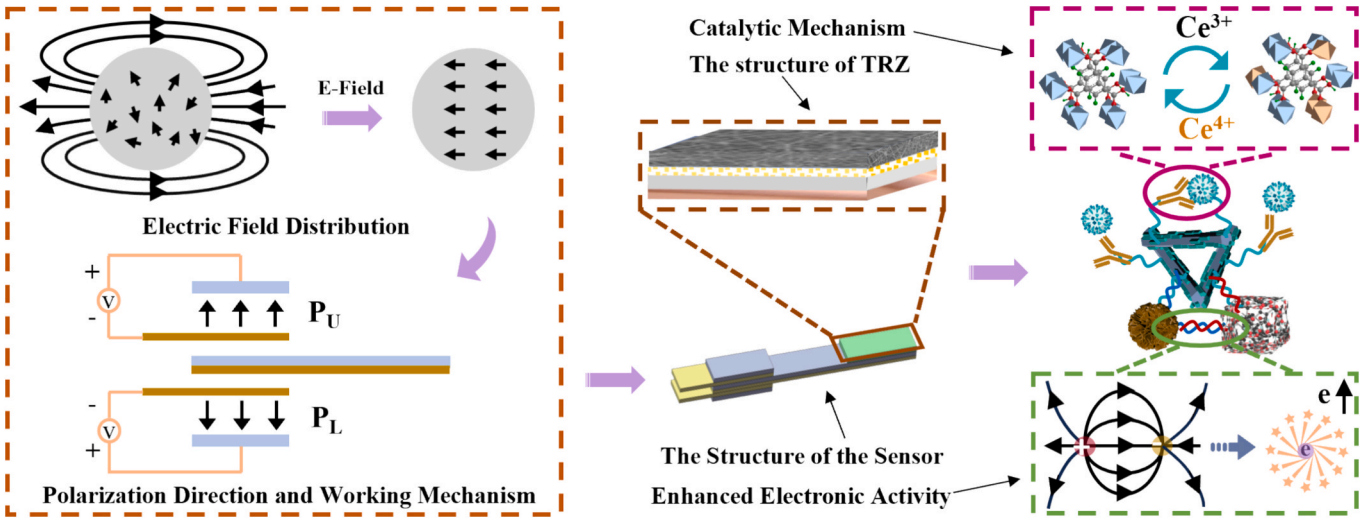

Fig. 8. Working mechanism diagram of the SASS-MS and reaction mechanism diagram of signal amplification strategy.

The reversible transformation between Ce^{3+} and Ce^{4+} in Ce(III, IV)-MOF provides it with significant redox ability, accompanied by charge transfer during the redox process (Equation (3) and (4)).

$$Ce^{4+} + e^- \rightarrow Ce^{3+} \quad (3)$$

$$Ce^{3+} + O_2 \rightarrow O_2^- + Ce^{4+} \quad (4)$$

Thus, Ce(III, IV)-MOF can also catalyze the redox reaction of CuNPs, thereby enhancing the conductivity of the conductive network, as shown in Equation (5) and (6) [38].

$$Cu + 2OH^- \rightarrow Cu(OH)_2 + 2e^- \quad (5)$$

$$Cu^{2+} + 2e^- \rightarrow Cu^0 \quad (6)$$

This catalytic effect was further validated by CV and XPS analyses. As shown in Fig. S6a, the CV curve of pure CuNPs exhibits a pair of characteristic redox peaks at approximately −0.40 V (reduction) and 0.10 V (oxidation), while Ce(III, IV)-MOF shows its redox peaks at around −0.30 V (reduction) and 0.30 V (oxidation). In contrast, the CuNPs@Ce(III, IV)-MOF composite displays multiple redox peaks at −0.40 V, −0.30 V, and −0.20 V (reduction), and 0.00 V, 0.10 V, and 0.35 V (oxidation), with significantly enhanced current response. Furthermore, XPS analysis provided additional evidence for this redox interaction. As shown in Fig. 3c and Fig. S6b, the Cu 2p spectrum of rGO-COOH@CuNPs shows a higher amount of Cu^{2+} (Fig. 3c), whereas after reacting with Ce(III, IV)-MOF, the Cu^{2+} content decreases and Cu(0) increases (Fig. S6b). Simultaneously, the Ce 3d spectra (before reaction in Fig. 3g, and after reaction in Fig. S6c) reveal an increase in Ce^{4+} and a decrease in Ce^{3+}. Experimental results indicate that Ce(III, IV)-MOF possesses multivalent redox capability, which can influence the valence state of Cu and promote the redox process of CuNPs through electron transfer, thereby validating its catalytic mechanism to a certain extent.

Additionally, the strong redox ability of Ce(III, IV)-MOF may improve the conformation of antibodies or enhance the affinity of antigens, facilitating their activation and subsequent binding. Moreover, Ce(III, IV)-MOF may improve antigen–antibody interactions and enhance binding efficiency through mechanisms involving surface functional groups, surface charge effects, and optimized binding sites.

3.6. Real sample analysis

To assess the applicability of the SASS-MS for detecting ALV-J in real samples, recovery experiments were performed using both chicken serum (CS) and vaginal swab (VS) samples. Various concentrations of Ag_{p27} were spiked into normal CS and VS samples and subsequently analyzed using the SASS-MS. The results were then compared with those obtained from enzyme-linked immunosorbent assay (ELISA). Recovery rates were calculated according to Equation (7).

$$Recovery = \frac{Found}{Added} \times 100\% \quad (7)$$

As shown in Table 2, the recovery rates of the SASS-MS ranged from 95.07 % to 103.88 % for CS and 91.06 % to 97.81 % for VS. ELISA showed a slightly higher recovery range of 94.24 % to 106.57 % for CS and 93.86 % to 99.12 % for VS. The data indicate that the SASS-MS maintained stable detection performance across different samples. However, the recovery rates for VS samples were slightly lower than those for CS, possibly due to matrix effects from vaginal secretions. Overall, both methods demonstrated high detection accuracy and reliability in detecting ALV-J in CS and VS samples.

4. Conclusion

In summary, this study presents a novel self-actuating and self-sensing microcantilever sensor, which successfully integrates piezoelectric actuator and sensing functionalities using piezoelectric ceramic (PZT) as the substrate, along with rGO-COOH@CuNPs@Ce(III, IV)-MOF nanocomposites for signal amplification. This innovative approach demonstrates effective detection of Avian Leukosis Viruses subgroup J (ALV-J), enabling rapid detection within seconds with high sensitivity and specificity, and significantly outperforming traditional ELISA methods. Furthermore, the study establishes a multi-functional detection platform, integrating advanced instrumentation, software, and computer vision techniques, which can be applied to the monitoring of various piezoelectric sensors with enhanced sensitivity and real-time monitoring. The sensor exhibits a detection range of 2.1×10^{-1} to 1.0×10^{1} ng mL^{-1} and a limit of detection of 1.3×10^{-1} ng mL^{-1}, along with satisfactory long-term storage stability and reproducibility (RSD = 3.57 %). These results highlight the potential of the self-actuating and self-sensing microcantilever sensor as a powerful tool for clinical diagnostics.

Table 2
Comparison of the SASS-MS and ELISA for detecting ALV-J in chicken serum and vaginal swab samples (n = 5, initial ALV-J content = 0).

NO.	Added (ng mL^{-1})	Samples	SASS-MS		ELISA	
			Found ± SD[a] (ng mL^{-1})	Recovery (%)	Found ± SD[a] (ng mL^{-1})	Recovery (%)
1	0.21	CS	0.20 ± 0.01	95.07	0.21 ± 0.07	100.54
		VS	0.19 ± 0.02	91.06	0.20 ± 0.06	95.24
2	0.85	CS	0.88 ± 0.04	103.88	0.88 ± 0.02	103.97
		VS	0.83 ± 0.05	97.81	0.84 ± 0.04	99.02
3	3.39	CS	3.22 ± 0.09	95.28	3.19 ± 0.12	94.24
		VS	3.16 ± 0.11	93.17	3.21 ± 0.13	93.86
4	8.45	CS	8.76 ± 0.33	103.64	9.01 ± 0.31	106.57
		VS	8.23 ± 0.39	97.43	8.39 ± 0.34	99.12

a) Standard deviation.

CRediT authorship contribution statement

Yongbin Qin: Writing – review & editing, Writing – original draft, Visualization, Validation, Software, Funding acquisition, Formal analysis, Data curation, Conceptualization. **Zichen Zheng:** Writing – review & editing, Writing – original draft, Visualization, Validation, Supervision, Funding acquisition, Data curation, Conceptualization. **Wei Gu:** Writing – review & editing, Writing – original draft, Visualization, Validation, Data curation. **Carla Bittencourt:** Writing – review & editing, Writing – original draft, Visualization, Validation. **Yani Jiang:** Supervision. **Lifeng Zhang:** Writing – review & editing, Writing – original draft, Visualization, Validation, Supervision, Software, Funding acquisition. **Yixiang Bian:** Writing – review & editing, Validation, Supervision, Funding acquisition, Conceptualization.

Declaration of competing interest

The authors declare that they have no known competing financial interests or personal relationships that could have appeared to influence the work reported in this paper.

Acknowledgments

The authors express sincere gratitude to Prof. Aijian Qin and Dr. Moru Xu from the Ministry of Education Key Lab for Avian Preventive Medicine at Yangzhou University for providing the antigens and antibodies of ALV-J, as well as for their guidance during the experiment.

This study was funded by the National Natural Science Foundation of China (No. 51775483), the Postgraduate Research & Practice Innovation Program of Jiangsu Province of China (No. KYCX24_3737 and No. KYCX23_3551), National Key Research and Development Program of China (2024YFD2000203) and the China Scholarship Council (No. 202308320445).

Appendix A. Supplementary data

Supplementary data to this article can be found online at https://doi.org/10.1016/j.cej.2025.162755.

Data availability

Data will be made available on request.

References

[1] M.R. Xu, F.S. Hang, K. Qian, H.X. Shao, J.Q. Ye, A.J. Qin, Chicken hepatomegaly and splenomegaly associated with novel subgroup J avian leukosis virus infection, BMC Vet. Res. 18 (1) (2022) 32, https://doi.org/10.1186/s12917-022-03139-1.

[2] H.J. Li, P.K. Wang, L.L. Lin, M.Y. Shi, Z.M. Gu, T. Huang, M.L. Mo, T.C. Wei, H. M. Zhang, P. Wei, The emergence of the infection of subgroup J avian leucosis virus escalated the tumour incidence in commercial Yellow chickens in Southern China in recent years, Transbound Emerg Dis. 66 (1) (2019) 312–316, https://doi.org/10.1111/tbed.13023.

[3] F.F. Chang, L.X. Xing, Z.F. Xing, M.M. Yu, Y.L. Bao, S.Y. Wang, M. Farooque, X. Y. Li, P. Liu, Q. Pan, X.L. Qi, L. Gao, K. Li, C.J. Liu, Y.P. Zhang, H.Y. Cui, X. M. Wang, Y.L. Gao, Development and evaluation of a gp85 protein-based subgroup-specific indirect enzyme-linked immunosorbent assay for the detection of anti-subgroup J avian leukosis virus antibodies, Appl. Microbiol. Biotechnol. 104 (4) (2020) 1785–1793, https://doi.org/10.1007/s00253-019-10320-4.

[4] L. Li, W.G. Feng, Z.Q. Cheng, J. Yang, J.M. Bi, X.M. Wang, G.H. Wang, TRIM62-mediated restriction of avian leukosis virus subgroup J replication is dependent on the SPRY domain, Poult. Sci. 98 (11) (2019) 6019–6025, https://doi.org/10.3382/ps/pez408.

[5] Y. Xiang, L.Z. Li, P. Liu, L. Yan, Z. Jiang, Y. Yu, Y. Li, X.Y. Chen, W.S. Cao, Rapid detection of avian leukosis virus subgroup J by cross-priming amplification, Sci. Rep. 11 (1) (2021) 10946, https://doi.org/10.1038/s41598-021-90479-x.

[6] L.L. Cao, P.P. Zhao, H. Ding, N. Wang, X. Zhang, S.X. Yuan, H. Dong, Y.B. Guo, X. H. Yao, Q.L. Yu, H.Z. Shao, P.T. Gong, Development of a double antibodies sandwich ELISA for the detection of avian leukosis virus subgroup J based on monoclonal antibodies against gp85, Acta Biochim. Biophys. Sin. 53 (10) (2021) 1408–1411, https://doi.org/10.1093/abbs/gmab114.

[7] U. Sungkanak, A. Sappat, A. Wisitsoraat, C. Promptmas, A. Tuantranont, Ultrasensitive detection of vibrio cholerae O1 using microcantilever-based biosensor with dynamic force microscopy, Biosens. Bioelectron. 26 (2) (2010) 784–789, https://doi.org/10.1016/j.bios.2010.06.024.

[8] S.Q. Wu, T.G. Nan, C.G. Xue, T. Cheng, H. Liu, B.M. Wang, Q.C. Zhang, X.P. Wu, Mechanism and enhancement of the surface stress caused by a small-molecule antigen and antibody binding, Biosens. Bioelectron. 48 (2013) 67–74, https://doi.org/10.1016/j.bios.2013.03.086.

[9] H.F. Ji, B.D. Armon, Approaches to increasing surface stress for improving signal-to-noise ratio of microcantilever sensors, Anal. Chem. 82 (5) (2010) 1634–1642, https://doi.org/10.1021/ac901955d.

[10] G.H. Wu, R.H. Datar, K.M. Hansen, T. Thundat, R.J. Cote, A. Majumdar, Bioassay of prostate-specific antigen (PSA) using microcantilevers, Nat. Biotechnol. 19 (9) (2001) 856–860, https://doi.org/10.1038/nbt0901-856.

[11] O. Mitsuhiro, W. Keisuke, A study of the electric power generation properties of a lead zirconate titanate piezoelectric ceramic, Ceram. Int. 42 (12) (2016) 14049–14060, https://doi.org/10.1016/j.ceramint.2016.06.012.

[12] T.L. Zhang, G. Zhao, J.r. Chu, W.H. Huang, M. Bartenwerfer, V. Eichhorn, S. Fatikow, Fabrication and characterization of piezoelectric cantilever array with nano-assembly carbon nanotube tips, in: V. Eichhorn, H. Xie, R. Liu, M.M. Yu (Eds.) 2012 International Conference on Manipulation, Manufacturing and Measurement on the Nanoscale (3M-NANO), IEEE, Xi'an, 2012, p. 292. https://doi.org/10.1109/3M-NANO.2012.6472929.

[13] J.Y. Zhao, F.Q. Han, C.F. Cheng, H.X. Wang, G.H. Zhao, P. Jia, N. Zhang, Y. G. Wang, J. Zhang, Q. Wei, Recent progress in noble metal-based single-atom nanozymes for biomedical applications, Microchem. J. 207 (2024) 111731, https://doi.org/10.1016/j.microc.2024.111731.

[14] C.F. Cheng, F.Q. Han, H.Y. Zhou, H.X. Wang, J.Y. Zhao, G.H. Zhao, Y. Zhang, N. Zhang, Y.G. Wang, M.M. Luan, Q. Wei, Construction of electrochemical immunosensors based on Au@MXene and Au@CuS nanocomposites for sensitive detection of carcinoembryonic antigen, Talanta 283 (2025) 127147, https://doi.org/10.1016/j.talanta.2024.127147.

[15] Y.Y. Wang, F.Q. Han, C.F. Cheng, J.Y. Zhao, C.X. Li, N. Zhang, Y.G. Wang, G. H. Zhao, Q. Wei, Electrochemical immunosensor utilizing Zn-Fe-N-C single-atom nanozyme and Ti3C2Tx@Au for ultrasensitive detection of cytokeratins21-1, Microchem. J. 209 (2025) 112810, https://doi.org/10.1016/j.microc.2025.112810.

[16] R.R. Shi, W.T. Zou, Z.L. Zhao, G.Q. Wang, M. Guo, S.Y. Ai, Q. Zhou, F.C. Zhao, Z. Y. Yang, Development of a sensitive phage-mimotope and horseradish peroxidase based electrochemical immunosensor for detection of O,O-dimethyl organophosphorus pesticides, Biosens. Bioelectron. 218 (2022) 114748, https://doi.org/10.1016/j.bios.2022.114748.

[17] G.J. Chen, Y. Qin, L. Jiao, J.J. Huang, Y. Wu, L.Y. Hu, W.L. Gu, D.C. Xu, C.Z. Zhu, Nanozyme-activated synergistic amplification for ultrasensitive photoelectrochemical immunoassay, Anal. Chem. 93 (17) (2021) 6881–6888, https://doi.org/10.1021/acs.analchem.1c01217.

[18] Z.H. Zhang, H.F. Ji, Y.P. Song, S. Zhang, M.H. Wang, C.C. Jia, J.Y. Tian, L.H. He, X. J. Zhang, C.S. Liu, Fe(III)-based metal–organic framework-derived core–shell nanostructure: sensitive electrochemical platform for high trace determination of heavy metal ions, Biosens. Bioelectron. 94 (2017) 358–364, https://doi.org/10.1016/j.bios.2017.03.014.

[19] G.L. Yang, X.L. Jiang, H. Xu, B. Zhao, Applications of MOFs as luminescent sensors for environmental pollutants, Small 17 (22) (2021), https://doi.org/10.1002/smll.202005327.

[20] G.H. Zhao, X. Dong, Y. Du, N. Zhang, G.Z. Bai, D. Wu, H.M. Ma, Y.G. Wang, W. Cao, Q. Wei, Enhancing electrochemiluminescence efficiency through introducing atomically dispersed ruthenium in nickel-based metal–organic frameworks, Anal. Chem. 94 (29) (2022) 10557–10566, https://doi.org/10.1021/acs.analchem.2c02334.

[21] W.L. Chen, Q. Zhu, Q.H. Tang, K. Zhao, A.P. Deng, J.G. Li, Ultrasensitive detection of diclofenac based on electrochemiluminescent immunosensor with multiple signal amplification strategy of palladium attached graphene oxide as bioprobes and ceria doped zinc oxide as substrates, Sens. Actuators, B. 268 (2018) 411–420, https://doi.org/10.1016/j.snb.2018.04.106.

[22] Y.H. Xiong, S.H. Chen, F.G. Ye, L.J. Su, C. Zhang, S.F. Shen, S.L. Zhao, Synthesis of a mixed valence state Ce-MOF as an oxidase mimetic for the colorimetric detection of biothiols, Chem. Commun. 51 (22) (2015) 4635–4638, https://doi.org/10.1039/C4CC10346G.

[23] L.F. Chen, H.Y. Zheng, X. Zhu, Z.Y. Lin, L.H. Guo, B. Qiu, G.N. Chen, Z.N. Chen, Metal–organic frameworks-based biosensor for sequence-specific recognition of double-stranded DNA, Analyst 138 (12) (2013) 3490–3493, https://doi.org/10.1039/C3AN00426K.

[24] Z.G. Hu, Y.X. Wang, D. Zhao, The chemistry and applications of hafnium and cerium(IV) metal–organic frameworks, Chem. Soc. Rev. 50 (7) (2021) 4629–4683, https://doi.org/10.1039/D0CS00920B.

[25] P.F. Shi, Y.C. Zhang, Z.P. Yu, S.S. Zhang, Label-free electrochemical detection of ATP based on amino-functionalized metal-organic framework, Sci. Rep. 7 (1) (2017) 6500, https://doi.org/10.1038/s41598-017-06858-w.

[26] X.R. Shao, X.Z. Song, X. Liu, L.G. Yan, L. Liu, D.W. Fan, Q. Wei, H.X. Ju, A dual signal-amplified electrochemiluminescence immunosensor based on core-shell CeO2-Au@Pt nanosphere for procalcitonin detection, Microchim. Acta. 188 (10) (2021) 344, https://doi.org/10.1007/s00604-021-04988-7.

[27] Y.G. Wang, G.H. Zhao, H. Chi, S.H. Yang, Q.F. Niu, D. Wu, W. Cao, T.D. Li, H. M. Ma, Q. Wei, Self-luminescent lanthanide metal–organic frameworks as signal probes in electrochemiluminescence immunoassay, J. Am. Chem. Soc. 143 (1) (2021) 504–512, https://doi.org/10.1021/jacs.0c12449.

[28] W.J. Yin, J.X. Zhang, H. Wang, Y. Wang, X. Zeng, Z.L. Xu, J.Y. Yang, Z.L. Xiao, B. D. Hammock, P. Wen, A highly sensitive electrochemical immunosensor based on electrospun nanocomposite for the detection of parathion, Food Chem. 404 (2023) 134371, https://doi.org/10.1016/j.foodchem.2022.134371.

[29] S. Velanki, S. Kelly, T. Thundat, D.A. Blake, H.F. Ji, Detection of Cd(II) using antibody-modified microcantilever sensors, Ultramicroscopy 107 (12) (2007) 1123–1128, https://doi.org/10.1016/j.ultramic.2007.01.011.

[30] Y.W. Zhang, F. Shi, C.G. Zhang, X. Sheng, Y.H. Zhong, H. Chong, Z.J. Yang, C. Y. Wang, Detection of avian influenza virus H9N2 based on self-driving and self-sensing microcantilever piezoelectric sensor, Chin. Chem. Lett. 34 (4) (2023) 107700, https://doi.org/10.1016/j.cclet.2022.07.043.

[31] Y.P. Dai, T. Wang, X.Y. Hu, S.Z. Liu, M. Zhang, C.Y. Wang, Highly sensitive microcantilever-based immunosensor for the detection of carbofuran in soil and vegetable samples, Food Chem. 229 (2017) 432–438, https://doi.org/10.1016/j.foodchem.2017.02.093.

[32] Y.P. Dai, Z.P. Ji, C.Y. Wang, X.Y. Hu, G.X. Wang, Microcantilever Biosensors, Prog. Chem. 28 (5) (2016) 697–710, https://doi.org/10.7536/PC151118.

[33] D. Xu, L. Liu, J. Guan, J.Y. Xu, T. Wang, A.J. Qin, X.Y. Hu, C.Y. Wang, Label-free microcantilever-based immunosensors for highly sensitive determination of avian influenza virus H9, Microchim. Acta. 181 (3–4) (2014) 403–410, https://doi.org/10.1007/s00604-013-1129-x.

[34] C.Y. Wang, D.Y. Wang, Y.D. Mao, X.Y. Hu, Ultrasensitive biochemical sensors based on microcantilevers of atomic force microscope, Anal. Biochem. 363 (1) (2007) 1–11, https://doi.org/10.1016/j.ab.2006.12.010.

[35] Y.S. Liu, Y.H. Zhong, C.Y. Wang, Recent advances in self-actuation and self-sensing materials: state of the art and future perspectives, Talanta 212 (2020) 120808, https://doi.org/10.1016/j.talanta.2020.120808.

[36] Y.N. Jiang, Y.B. Qin, S.E. Lu, Z. Wang, Q. Li, Y.X. Bian, Outcomes of the bionic semicircular canals support the "density hypothesis" and "circular hypothesis", Rev. Sci. Instrum. 93 (3) (2022) 034105 https://doi.org/10.1063/5.0061752.

[37] J.C. Liu, S.P. Xu, L. Liu, D.D. Sun, The size and dispersion effect of modified graphene oxide sheets on the photocatalytic H_2 generation activity of TiO_2 nanorods, Carbon 60 (2013) 445–452, https://doi.org/10.1016/j.carbon.2013.04.059.

[38] J. Xiong, Y. Wang, Q.J. Xue, X.D. Wu, Synthesis of highly stable dispersions of nanosized copper particles using l-ascorbic acid, Green Chem. 13 (4) (2011) 900–904, https://doi.org/10.1039/C0GC00772B.

[39] K.K.H. De Silva, H.H. Huang, M. Yoshimura, Progress of reduction of graphene oxide by ascorbic acid, Appl. Surf. Sci. 447 (2018) 338–346, https://doi.org/10.1016/j.apsusc.2018.03.243.
[40] D.X. Ma, J.H. Liu, H.B. Liu, J.L. Yi, F.Q. Xia, D. Tian, C.L. Zhou, Multiplexed electrochemical aptasensor based on mixed valence Ce(III, IV)-MOF for simultaneous determination of malathion and chlorpyrifos, Anal. Chim. Acta. 1230 (2022) 340364, https://doi.org/10.1016/j.aca.2022.340364.
[41] A. Lerf, H. He, M. Forster, J. Klinowski, Structure of graphite oxide revisited, J. Phys. Chem. b. 102 (23) (1998) 4477–4482, https://doi.org/10.1021/jp9731821.
[42] X.F. Gao, J. Jang, S. Nagase, Hydrazine and thermal reduction of graphene oxide: reaction mechanisms, product structures, and reaction design, J. Phys. Chem. c. 114 (2) (2010) 832–842, https://doi.org/10.1021/jp909284g.
[43] K.C. Zuo, X.C. Huang, X.C. Liu, E.M. Gil Garcia, J. Kim, A. Jain, L. Chen, P. Liang, A. Zepeda, R. Verduzco, J. Lou, Q.L. Li, A hybrid metal–organic framework–reduced graphene oxide nanomaterial for selective removal of chromate from water in an electrochemical process, Environ. Sci. Technol. 54(20) (2020) pp13322-13332. Doi: 10.1021/acs.est.0c04703.
[44] Y. Gao, Y. Zhou, D.F. Dai, N. Sun, H.L. Tan, Z.L. Zhan, J.M. Cai, X.M. Cai, Controllable preparations and anti-corrosion properties of reduced graphene oxide films by binder-free electrophoretic deposition, Appl. Surf. Sci. 563 (2021) 150295, https://doi.org/10.1016/j.apsusc.2021.150295.
[45] L. Cai, J.N. Zhang, L.H. Teng, H.Y. Wang, G.Z. Fang, S. Wang, Ultrasensitive molecularly imprinted electrochemiluminescence sensor based on highly-conductive rGO-COOH synergically amplify TCPP luminophor signal in aqueous phase system for “switches-controlled” detection of tryptamine, Sens. Actuators, b. 366 (2022) 132004, https://doi.org/10.1016/j.snb.2022.132004.
[46] P. Wang, D.J. Wang, J. Song, Z.Y. Mao, Q.F. Lu, Incorporation of Si–O induced valence state variation of cerium ion and phase evolution in YAG:Ce phosphors for white light emitting diodes, J. Mater. Sci. - Mater. Electron. 23 (9) (2012) 1764–1769, https://doi.org/10.1007/s10854-012-0659-z.
[47] X. Su, Z.Y. Zhong, X.L. Yan, T. Zhang, C.Z. Wang, Y.X. Wang, G. Xu, L. Chen, Facile synthesis of metallosalphen-based 2D conductive metal-organic frameworks for NO_2 sensing: metal coordination induced planarization, Angew. Chem. Int. Ed. 62 (22) (2023) e202302645, https://doi.org/10.1002/anie.202302645.
[48] K. Liu, H.P. You, G. Jia, Y.H. Zheng, Y.J. Huang, Y.H. Song, M. Yang, L.H. Zhang, H.J. Zhang, Hierarchically nanostructured coordination polymer: Facile and rapid fabrication and tunable morphologies, Cryst. Growth Des. 10 (2) (2010) 790–797, https://doi.org/10.1021/cg901170j.
[49] Y.Y. Cheng, L. Liang, F.G. Ye, S.L. Zhao, Ce-MOF with intrinsic haloperoxidase-like activity for ratiometric colorimetric detection of hydrogen peroxide, Biosensors 11 (7) (2021) 204, https://doi.org/10.3390/bios11070204.
[50] Q. Huang, S.C. Zhang, X.X. Li, Y.Y. Wu, Y.H. Liu, J. Ran, P. Cui, C.F. Fu, L. Ding, T. W. Xu, Intelligent graphene oxide membranes with pH tunable channels for water treatment, Chem. Eng. J. 431 (2022) 133462, https://doi.org/10.1016/j.cej.2021.133462.
[51] X.J. Liu, L. Long, W.X. Yang, L.L. Chen, J.B. Jia, Facilely electrodeposited coral-like copper micro-/nano-structure arrays with excellent performance in glucose sensing, Sens. Actuators, b. 266 (2018) 853–860, https://doi.org/10.1016/j.snb.2018.04.007.
[52] W.L. Zhen, W.J. Jiao, Y.Q. Wu, H.W. Jing, G.X. Lu, The role of a metallic copper interlayer during visible photocatalytic hydrogen generation over a Cu/Cu_2O/Cu/TiO_2 catalyst, Catal. Sci. Technol. 7 (21) (2017) 5028–5037, https://doi.org/10.1039/C7CY01432E.
[53] S. Ma, D.J. Yang, S.J. Ding, J. Liu, W. Wang, Z.Y. Wu, X.D. Liu, L. Zhou, Q.Q. Wang, Tunable size dependence of quantum plasmon of charged gold nanoparticles, PhysRevLett.1 126 (17) (2021) 173902, https://doi.org/10.1103/PhysRevLett.126.173902.
[54] J.Y. Fu, X.S. An, Y. Yao, Y.M. Guo, X. Sun, Electrochemical aptasensor based on one step co-electrodeposition of aptamer and GO-CuNPs nanocomposite for organophosphorus pesticide detection, Sens. Actuators, b. 287 (2019) 503–509, https://doi.org/10.1016/j.snb.2019.02.057.
[55] K.W. Liu, Z.C. Zheng, M. Debliquy, C. Zhang, Highly-sensitive volatile organic compounds evaluation by three-dimensional $ZnFe_2O_4$/$ZnSnO_3$ heterostructures and their predictive grain quality monitoring, Chem. Eng. J. 453 (2023) 139824, https://doi.org/10.1016/j.cej.2022.139824.
[56] C. Zhang, Z.C. Zheng, K.W. Liu, M. Debliquy, Q.Q. Liu, Highly sensitive and selective Sb_2WO_6 microspheres in detecting VOC biomarkers in cooked rice: experimental and density functional theory study, Food Chem. 424 (2023) 136323, https://doi.org/10.1016/j.foodchem.2023.136323.
[57] N.X. Li, X.Y. Zou, M. Liu, L.F. Wei, Q.H. Shen, R. Bibi, C.J. Xu, Q.H. Ma, J.C. Zhou, Enhanced visible light photocatalytic hydrogenation of CO_2 into methane over a Pd/Ce-TiO_2 nanocomposition, J. Phys. Chem. c. 121 (46) (2017) 25795–25804, https://doi.org/10.1021/acs.jpcc.7b07298.
[58] C.F. Cheng, H.X. Wang, J.Y. Zhao, Y.Y. Wang, G.H. Zhao, Y. Zhang, X. Liu, Y. G. Wang, Advances in the application of metal oxide nanozymes in tumor detection and treatment, Colloids Surf., b. 235 (2024) 113767, https://doi.org/10.1016/j.colsurfb.2024.113767.
[59] F.Q. Han, C.F. Cheng, J.Y. Zhao, H.X. Wang, G.H. Zhao, Y. Zhang, N. Zhang, Y. G. Wang, J. Zhang, Q. Wei, Single-atom nanozymes: Emerging talent for sensitive detection of heavy metals, Colloids Surf., b. 242 (2024) 114093, https://doi.org/10.1016/j.colsurfb.2024.114093.
[60] Y.Y. Wang, Z.G. Li, P. Zhang, Y. Pan, Y. Zhang, Q. Cai, S.R.P. Silva, J. Liu, G. X. Zhang, X.M. Sun, Z.F. Yan, Flexible carbon nanofiber film with diatomic Fe-Co sites for efficient oxygen reduction and evolution reactions in wearable zinc-air batteries, Nano Energy 87 (2021) 106147, https://doi.org/10.1016/j.nanoen.2021.106147.
[61] B. Gao, Z.H. Yao, D.Y. Lai, Q.H. Guo, W.G. Pan, H. Hao, M.H. Cao, H.X. Liu, Unexpectedly high piezoelectric response in Sm-doped PZT ceramics beyond the morphotropic phase boundary region, J. Alloys Compd. 836 (2020) 155474, https://doi.org/10.1016/j.jallcom.2020.155474.
[62] S.X. Ning, M.Q. Zhou, C. Liu, G.I.N. Waterhouse, J. Dong, S.Y. Ai, Ultrasensitive electrochemical immunosensor for avian leukosis virus detection based on a β-cyclodextrin-nanogold-ferrocene host-guest label for signal amplification, Anal. Chim. Acta. 1062 (2019) 87–93, https://doi.org/10.1016/j.aca.2019.02.041.
[63] G.H. Wang, Y.M. Wang, Z.Q. Cheng, Immunochromatographic test (ICT) for the detection of antibody against ALV-J, Thai Journal of Veterinary Medicine. 52 (2) (2022) 373–376, https://doi.org/10.14456/tjvm.2022.42.
[64] M.M. Yu, Y.L. Bao, M.P. Wang, H.B. Zhu, X.Y. Wang, L.X. Xing, F.F. Chang, Y. Z. Liu, M. Farooque, Y.Q. Wang, X.L. Qi, C.J. Liu, Y.P. Zhang, H.Y. Cui, K. Li, L. Gao, Q. Pan, X.M. Wang, Y.L. Gao, Development and application of a colloidal gold test strip for detection of avian leukosis virus, Appl. Microbiol. Biotechnol. 103 (1) (2019) 427–435, https://doi.org/10.1007/s00253-018-9461-z.
[65] H.N. Wang, J.C. Guan, X.N. Liu, Y. Shi, Q.W. Wu, M.Z. Luo, Y.J. Zhu, Z.Z.C. Wang, L.F. Wang, Y. Pan, Rapid detection of avian leukosis virus using a fluorescent microsphere immunochromatographic test strip assay, Poult. Sci. 98 (12) (2019) 6492–6496, https://doi.org/10.3382/ps/pez547.
[66] J. Wang, X.Z. Qin, Z.M. Liu, G.Y. Ding, G.J. Cai, Experimental study on fatigue degradation of piezoelectric energy harvesters under equivalent traffic load conditions, Int. J. Fatigue. 150 (2021) 106320, https://doi.org/10.1016/j.ijfatigue.2021.106320.
[67] C. Singh, V.N. Thakur, A. Kumar, Investigation on barometric and hydrostatic pressure sensing properties of $Pb[(Mg_{1/3}Nb_{2/3})_{0.7}Ti_{0.3}]O_3$ electro-ceramics, Ceram. Int. 47(5) (2021) 6982-6987. https://doi.org/10.1016/j.ceramint.2020.11.047.